ORIGINAL CONTRIBUTION

A morphological approach to the automatic detection of dark fringes of birefringence images obtained in a multipass rheometer

Allan F. da Silva[1] · Lucas A. Thomaz[1,2] · Juliana O. Pereira[3] · André Castro[4] · Thais M. Farias[5] · Sergio L. Netto[1,6] · Eduardo A. B. da Silva[1,6] · Argimiro R. Secchi[3]

Abstract

This work presents a novel approach to automatically detect the position of dark fringes in birefringence images obtained during the flow of polymers through slit dies. The determination of these positions is important for rheology, as it allows one to obtain the principal stress difference (PSD) profile along the flow centerline. The developed approach uses mathematical morphology techniques to find the patterns that characterize the birefringence fringes and to detect their center position. The proposed method was compared with other fringe center detection methods, revealing the superior accuracy of our method, and the results were compared with the semi-automated measurements obtained with the GIMP software in a previous work. In addition, the statistical analysis performed showed that the difference of the average obtained with the two methodologies can be considered irrelevant to the application at hand for most of the fringes observed in the experiments.

Introduction

To understand a process which involves the flow of molten polymers, it is necessary to concentrate great effort in the modeling of the flow. It is also important to evaluate the experimental techniques used to obtain the different material functions to characterize the nonlinear response of these materials. In attempt to address this challenge,

rheo-optical techniques for determining the flow birefringence stress patterns can be coupled with sophisticated experimental apparatus, such as the multipass rheomoter (MPR) developed by Prof. Mackley and co-workers (Mackley and Hassell 2011; Lord et al. 2010; Hassell and Mackley 2009; Hassell et al. 2008; Collis and Mackley 2005; Lee and Mackley 2001). In this device, it is possible to map the stress field during the flow, when it is equipped with an optical cell designed to fit the different geometries. Besides the rheological characterization, these data are especially useful for the differentiation of grades (Farias et al. 2014), evaluation of molecular weight distribution (Collis and Mackley 2005) and branching of polymers (Hassell et al. 2011). Furthermore, flow-induced birefringence is used for the validation of constitutive models for the simulation of viscoelastic fluid flow with complex rheological behavior (see, for example, Hassell and Mackley (2009), Lord et al. (2010), Agassant and Mackley (2015), and Harrison et al. (2002)). Flow-induced birefringence is an interesting technique to identify the viscoelastic behavior of molten polymers. However, the birefringence index during flow needs to be suitable. Very low index results in a very small number of fringes, even at high flow velocities, whereas a very high index, as in the case of polystyrene studied, drastically limits the possible flow velocities investigated because of the large number of fringes observed.

✉ Juliana O. Pereira
  jpereira@peq.coppe.ufrj.br

[1] Programa de Engenharia Elétrica (PEE), Universidade Federal do Rio de Janeiro (UFRJ), Rio de Janeiro, Brazil

[2] Instituto de Telecomunicações (IT), Leiria, Portugal

[3] Programa de Engenharia Química (PEQ), Universidade Federal do Rio de Janeiro (UFRJ), Rio de Janeiro, Brazil

[4] Escola de Química (EQ), Universidade Federal do Rio de Janeiro (UFRJ), Rio de Janeiro, Brazil

[5] Departamento de Engenharia Química (DEQUI), Escola de Engenharia, Universidade Federal do Rio Grande do Sul (UFRGS), Porto Alegre, Brazil

[6] Departamento de Engenharia Eletrônica e de Computação (DEL), Escola Politécnica, Universidade Federal do Rio de Janeiro (UFRJ), Rio de Janeiro, Brazil

The experimental procedure is based on inducing a birefringence in a fluid as a result of orientation of the polymer chains during its flow. The obtained patterns of bright and dark fringes, which provide information about the spatial evolution of the stress in the molten polymer, can then be converted into the principal stress difference (PSD) profile using the semi-empirical stress optical rule (Castro et al. 2018; Farias et al. 2014; Collis and Mackley 2005; Lee and Mackley 2001; Ahmed et al. 1995; Macosko and Larson 1994; Harrison et al. 2002). Along the flow centerline, the PSD is equal to the first normal stress difference, that is,

$$|\text{PSD}| = |\sigma_{11} - \sigma_{22}| = |\tau_{11} - \tau_{22}| = \frac{k\lambda}{|C|d}, \qquad (1)$$

where σ_{11} and σ_{22} are the first principal stress values, τ_{11} and τ_{22} are the first normal stress values, C (stress optical coefficient) is $-4.5 \times 10^{-9}\,\text{Pa}^{-1}$ for polystyrene (Collis and Mackley 2005; Farias et al. 2014), $k = 0, 1, 2, \ldots$ is the fringe order, λ is the wavelength of the polarized light which hits the birefringent medium, and d is the anisotropic medium length, which corresponds to the depth of the sample through the light propagates, assuming a 2D-deformation flow.

Using Eq. 1 with the values of the parameters given by the experiment and knowing the geometry length and the position of the center of each dark fringe, the PSD along the centerline can be determined by counting the relative retardation of the fringe order k (see for example Lord et al. (2010), Hassell and Mackley (2009), Hassell et al. (2008), Collis and Mackley (2005), Lee and Mackley (2000), and Castro et al. (2018)).

Several aspects related to the processing of different types of polymer tested in the MPR rheometer have been discussed and presented during the last years (Lee and Mackley 2001; Hassell and Mackley 2009; Lord et al. 2010; Mackley and Hassell 2011; Hassell et al. 2011; Reynolds et al. 2018). However, in general, the available information is still insufficient to allow an effective understanding on how the determination of the dark fringes centers is performed.

In general, many methods studied fringe detection, specially in the context of light interference fields (Farooq et al. 2015; Ye and Wei 2012; Yu and Andresen 1994; EL-Morsy 2012; Sokkar et al. 2007; Poon et al. 1993; Huntley 1998; Fulong and Wang 1999; Wang and Han 2004; Meyer 1979). For example, a method based on image binarization creates a centerline of each fringe by employing morphological approaches like thinning or skeletonisation (Farooq et al. 2015). In other works, the periodic characteristics of the fringes are modulated by a signal (EL-Morsy 2012).

Some of the most successful techniques to detect light interferometric fringes (Yu and Andresen 1994; Zhang et al.

2002) rely on the estimation of an orientation map for each image, which is used with an adaptive median filter to remove noise. By measuring the changes in the gradient component along the direction given by the orientation map, one can define the positions of maxima and minima in the image, which characterizes the centerline for each light or dark fringe.

However, most of the methods developed for light interference fields tend to fail when applied to the case of birefringence images. In this scenario, the fringe patterns in the images are related to the flow and geometry of the experiment and some assumptions about the periodicity of the image do not hold. In addition, due to experimental problems such as impurities in the material and difficulties in the image acquisition, the resulting images are often corrupted by noise.

For the specific case of MPR optical images, Agassant et al. (2002) mentioned the application of a morphological analysis that considers a skeleton birefringence pattern to detect the position of the fringes. However, no further details are provided about the adopted approach.

Recently, Thomaz et al. (2016) proposed a group of mathematical morphology techniques to find the patterns that characterize the birefringence fringes obtained in the MPR4 (Collis and Mackley 2005; Hassell et al. 2008; Mackley and Hassell 2011; Farias et al. 2014). Their approach to detect the center position of each fringe contains five steps: (i) input image enhancement, (ii) minima contour detection with watershed, (iii) skeleton creation and center detection, (iv) post-processing, and (v) inflection points detection. The authors showed that the method has great potential for detecting dark fringes in birefringence images with accuracy prediction comparable to a manual marking while minimizing the need of human interaction with the images.

In a preliminary work (Castro et al. 2018), a semi-automated methodology was presented for PSD analysis from flow-induced birefringence images using the GIMP (GNU Image Manipulation Program) open-source software. The position of the centers of dark fringes obtained through the flow-induced birefringence images of two polystyrene samples processed in the MPR4 was determined with greater accuracy and with shorter processing time when compared with the standard manual technique. The main advantage of using the cited approach is that it does not require any prior knowledge of advanced image processing techniques nor the use of expensive computational packages. However, in such scheme, the user still performs the fringe processing and analysis one image at a time, resulting in a time consuming process.

Within the above context, this work aims to present a novel approach using mathematical morphology techniques that expands the work of Thomaz et al. (2016)

to identify the patterns that characterize the birefringence images presented by Castro et al. (2018). In addition, it also performs the automatic detection of the dark fringes centers, allowing the collection of measurements to be obtained in a faster and more accurate way. To introduce such methodology, the remaining of this paper is organized as follows: Section "Processing of birefringence images using mathematical morphology techniques" presents a step-by-step description of the fringe position detector based on mathematical morphology techniques. Section "Comparison with other fringe center detection methods" assesses the proposed methodology by comparing its results with the ones obtained with the manual technique, with the GIMP software, and with other methods adapted to the context of birefringence images (Lee and Mackley 2001; Collis and Mackley 2005; Fuller 1995; Lord et al. 2010; Castro et al. 2018). Finally, the conclusions are presented in "Conclusions" emphasizing the paper main technical contributions.

Mathematical morphology

Mathematical morphology is the study of the shape of spatial structures, often used to remove imperfections or identify patterns (Serra 1983). It provides tools to analyze the relationship between the pixel values of an image, considering their spatial ordering and a small template called structuring element. These interactions between an image and a structuring element are explored using two basic operations, namely erosion and dilation (Soille 2003).

The erosion of an image $\mathbf{f}$ using a structuring element $\mathbf{B}$ can be defined as follows. One starts assuming that $\mathbf{f}$ and $\mathbf{B}$ exist in the same two-dimensional Euclidian space, where $\mathbf{f}$ is a grayscale image and $\mathbf{B}$ is a structuring element that is defined as a binary set.

The eroded value of $\mathbf{f}$ for each pixel $\mathbf{x}$ is the minimum intensity value inside the window delimited by the structuring element $\mathbf{B}$. If $\mathbf{b}$ is a translation belonging to the structuring element, the eroded image $\varepsilon_{\mathbf{B}}(\mathbf{f})$ is equal to the following:

$$\text{Erosion: } [\varepsilon_{\mathbf{B}}(\mathbf{f})](\mathbf{x}) = \min_{\mathbf{b} \in \mathbf{B}} \mathbf{f}(\mathbf{x} + \mathbf{b}) \qquad (2)$$

Similarly, the dilation operation of $\mathbf{f}$ by $\mathbf{B}$, which is the dual operation of the erosion, is defined for each pixel $\mathbf{x}$ as the maximum value of the image intensity value in the window defined by the structuring element $\mathbf{B}$, leading to the following:

$$\text{Dilation: } [\delta_{\mathbf{B}}(\mathbf{f})](\mathbf{x}) = \max_{\mathbf{b} \in \mathbf{B}} \mathbf{f}(\mathbf{x} + \mathbf{b}) \qquad (3)$$

Examples of the erosion and dilation operations are depicted, respectively, in Fig. 1c, d, where it can be observed that the erosion shrinks the objects while the dilation enlarges them.

The erosion and dilation operations can be used to define more complex morphological operations, among which we can mention the opening and closing operations, widely used in morphological processing (Soille 2003). The opening consists of an erosion of $\mathbf{f}$ by the structuring element $\mathbf{B}$, followed by a dilation using the same structuring element. The following equation describes it as follows:

$$\text{Opening: } \gamma_{\mathbf{B}} = \delta_{\mathbf{B}}[\varepsilon_{\mathbf{B}}(\mathbf{f})]. \qquad (4)$$

The closing operation is the dual to the opening operation, and is performed by applying a dilation of $\mathbf{f}$ by the structuring element $\mathbf{B}$ followed by a erosion using the same structuring element. It is equivalent to applying the opening to the complement of the original image, and then taking the complement of the result, as shown in the following equation:

$$\text{Closing } \phi_{\mathbf{B}} = \varepsilon_{\mathbf{B}}[\delta_{\mathbf{B}}(\mathbf{f})]. \qquad (5)$$

Figure 1e and f show, respectively, examples for the opening and closing operation. One can see that the opening removes the image tips while the dilation fills the image holes (which is equivalent to removing the tips on the complement of the image).

Geodesic morphology

The basic morphology operations consider only an input image and computes its relation with a structuring element. Geodesic transformations (Soille 2003) consider instead two input images: the original input image, called marker, and a second image which acts as a mask. A morphological transformation is applied to the marker image, using a simple structuring element. However, if for a given position, the result is bigger or smaller than the mask, depending on the operation, it is set as the value of the mask.

A geodesic erosion of size 1 consists of a morphological erosion of a marker image $\mathbf{f}$ using an elementary isotropic structuring element $\mathbf{B}$, such as the one given by Fig. 1b, followed by a pointwise maximum between the result and the mask $\mathbf{g}$, as follows:

$$\text{Geodesic erosion: } \varepsilon_g^{(1)}(\mathbf{f}) = \varepsilon^{(1)}(\mathbf{f}) \vee \mathbf{g}, \qquad (6)$$

where $a \vee b$ represents the maximum value between a and b. This operation is depicted in Fig. 2d, e, which show that the geodesic erosion uses the mask to limit the shrinkage effect caused by the erosion (see Fig. 1c).

A geodesic dilation of size 1 consists of a morphological dilation of a marker image $\mathbf{f}$ using an elementary structuring element $\mathbf{B}$, followed by a pointwise minimum between the result and the mask $\mathbf{g}$, as follows:

$$\text{Geodesic dilation: } \delta_g^{(1)}(\mathbf{f}) = \delta^{(1)}(\mathbf{f}) \wedge \mathbf{g}, \qquad (7)$$

Fig. 1 Erosion, dilation, opening, and closing operations. **a** Original image. The pixel values for a section of image are represented as gray bars. **b** Structuring element defining a window for the maximum and minimum operations, consisting of one pixel to the left, the current pixel, and one pixel to the right. **c** Erosion: the object is reduced (the regions with low gray levels are enlarged). **d** Dilation: the object is enlarged in the borders (the regions with high gray levels are enlarged). **e** Opening: the holes in the gray level are removed. **f** Closing: the holes in the gray level are filled. In (**c**)–(**f**), the solid lines represent the values of the original image before the morphological operations and the gray rectangles show the result after each operation
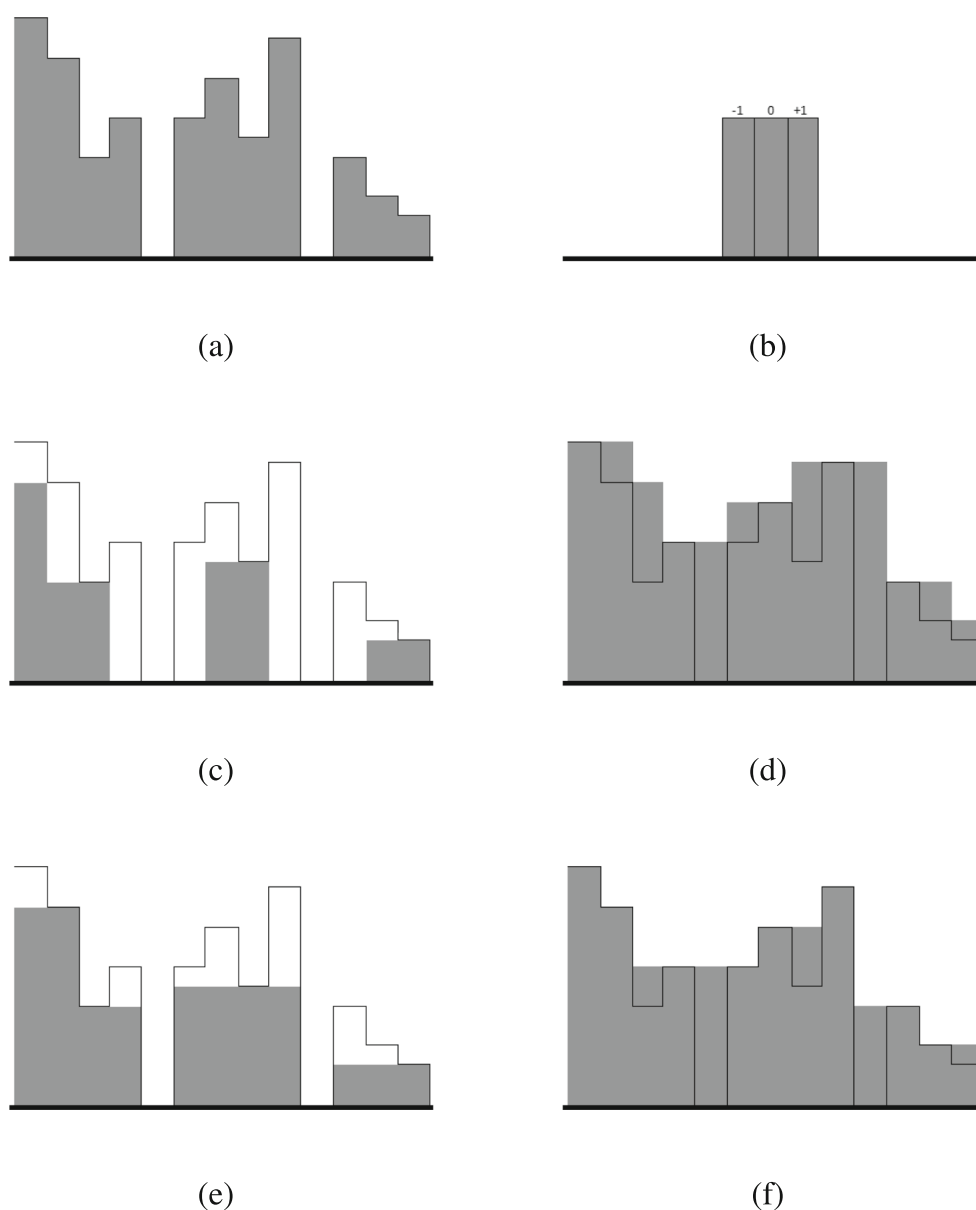
where $a \wedge b$ represents the minimum value between a and b. An example of this operation is shown in Fig. 2b, c, where one can see that, when compared to the dilation seen in Fig. 1d, the geodesic dilation forces the dilation process to propagate the image only to regions delimited by the mask.

Processing of birefringence images using mathematical morphology techniques

In this work, we propose a method to automatically detect the dark fringes in the birefringence patterns, which is an improvement to the four-step approach that was introduced in Thomaz et al. (2016). This approach differs from other, more traditional, methods as it works strictly on the geometrical domain, avoiding the use of more complex tools that can also be more error prone, such as frequency-domain techniques and transformations (Farooq et al. 2015; Yu and Andresen 1994; Zhang et al. 2002). A block diagram summarizing the workflow of the proposed method is presented in Fig. 3. The first step consists of an image enhancement that removes some of the image noise, providing a sharper version of the input image that allows a more precise detection in the subsequent steps. In the second step, the minima contours are detected through the application of the watershed (Beucher and Lantuéj 1979) method, further detailed. A skeleton (Haralick and Shapiro 1992) of the dark fringes is created from the previous step output and the center of the image, which is the region of

Fig. 2 Geodesic erosion and dilation operations. **a** Original image - marker image. The pixel values for a section of image are represented as gray bars. **b** Mask image used in the geodesic erosion, whose values are given by the solid black lines. The gray rectangles show the marker image, for comparison. **c** Geodesic erosion: erosion of the marker image. The mask prevents the decrease in the marker (the enlargement of regions with low gray values) caused by the erosion, when compared to Fig. 1c. **d** Mask image used in the geodesic dilation, whose values are given by the solid black lines. The gray rectangles show the marker image, for comparison. **e** Geodesic dilation: dilation of the marker image. The mask prevents the growth in the marker (the enlargement of the regions with high gray values) caused by the dilation, when compared to Fig. 1d

(a)

(b)

(c)

(d)

(e)
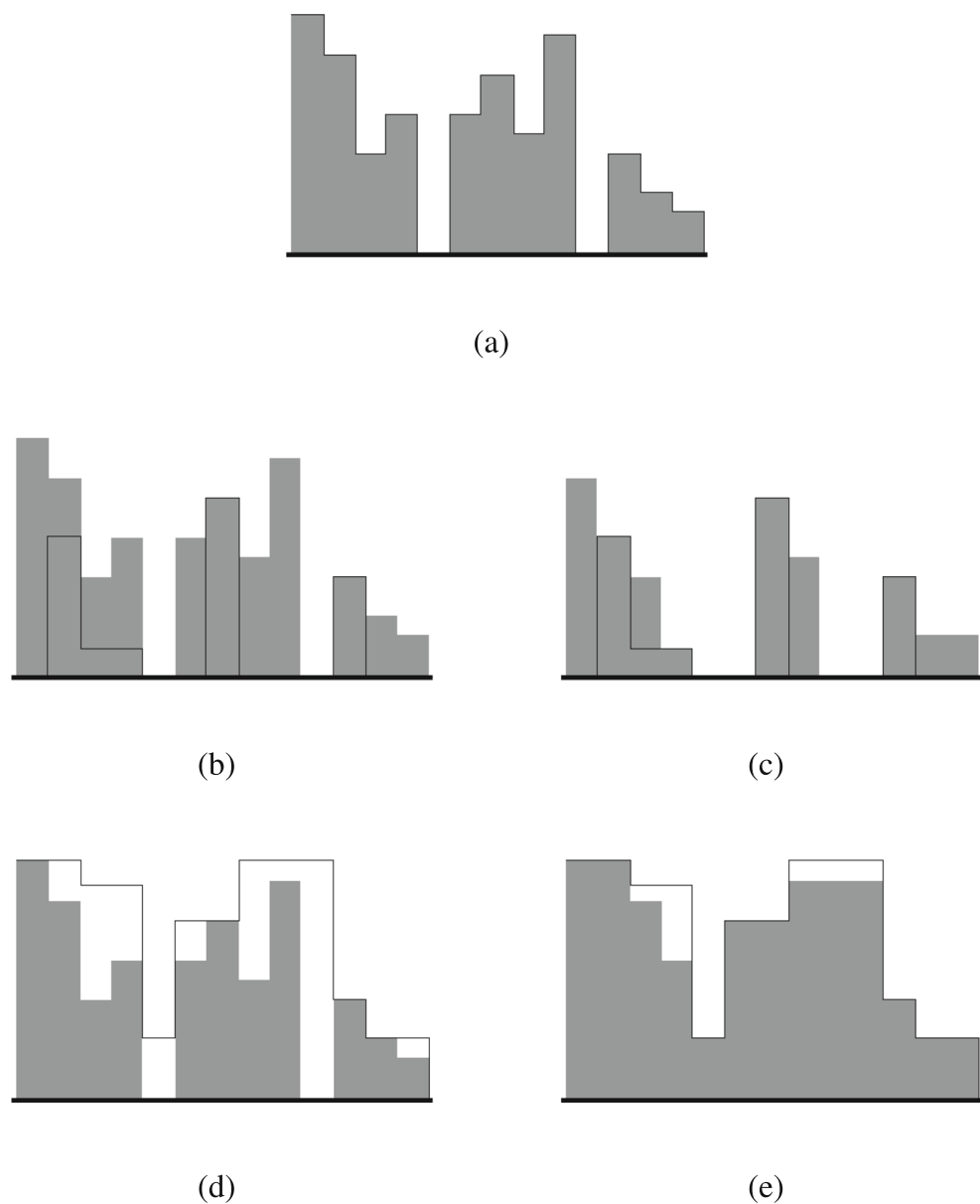
interest for the fringe position detection, is selected in the third step. Finally, in step four, post-processing is performed to increase the precision on the dark-fringe final detection. A detailed explanation of each of those steps is given in the subsections that follow.

Input image enhancement

To obtain a improved version of the image, thus improving the detection algorithm results, this section describes an image enhancement method that is applied in the proposed algorithm as a pre-processing step (Fig. 4).

Due to a noisy acquisition process, the birefringence images often have a cracked appearance, as can be seen in

Fig. 5. There it can be observed that neither their white nor their dark fringes are well defined, having many gaps that can connect consecutive dark fringes. They make the task of correctly identifying the fringes position very difficult for the image processing algorithms. One way to approach this hard problem is to apply some morphological operations on the input images as a pre-processing step (Fig. 4) that aims to highlight the fringe silhouettes, thus making the algorithms less prone to errors.

In this paper, we propose to use two morphological operations in succession to improve the image quality, namely *white top-hat* and *black top-hat*. The white top-hat operation (Soille 2003) aims to obtain the peak grayscale values of the image by applying morphological operations
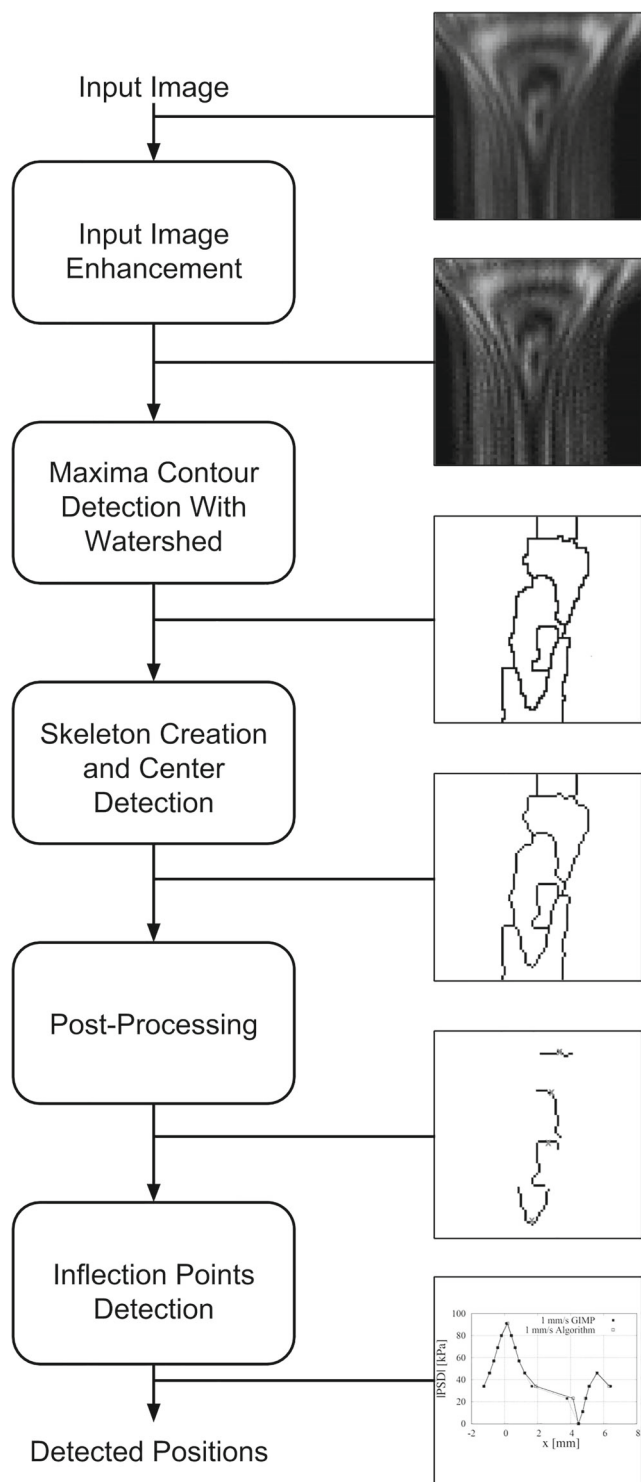
Fig. 3 Block diagram of the proposed method

over it. In order to do so a modified version of the image, obtained via the morphological opening operation defined in "Mathematical morphology" is subtracted from the original image, as described by the following:

White top-hat: $\mathrm{WTH}(\mathbf{f}) = f - \gamma(\mathbf{f}),$ (8)

where $\gamma()$ represents the opening operation.

The idea behind this operation is that, as shown in Fig. 1e, the opening removes the peaks in the shape of the objects, keeping the parts of the object that do not contain peaks. The white top-hat operation then takes the original image and subtracts from it a version of the image with the peaks removed, so after the subtraction only the peaks remain.

In the opposite way, the black top-hat operation (Soille 2003) is responsible for extracting the valleys of the gray level images. To perform this operation, the original image is subtracted from a modified version of the image, after going through a closing operation, is given by the following:

Black top-hat: $\mathrm{BTH}(\mathbf{f}) = \phi(\mathbf{f}) - \mathbf{f},$ (9)

where $\phi()$ represents the closing operation.

This equation means that first the closing operation is applied to create a version of the image with all valleys filled, such as the one seen in Fig. 1f. Afterwards, by subtracting this result from the original image, only the filled valleys remain, so the result of the black top-hat operation is an image containing only the valleys of the original image.

The resulting images after the described procedures, that are the white top-hat image containing the peaks and the black top-hat image containing the valleys, are added to the original image, emphasizing the peaks and valleys of the grayscale image, therefore enhancing its contrast. The use of these techniques yields a better distinction between the bright and dark fringes, as illustrated in Fig. 6.

Minima contour detection with watershed

Since the current state of the image is still not easy to process, in order to locate the minima contours of the pre-processed image, we apply the watershed operation as described in this section.

In order to detect the center of each dark fringe (Fig. 7), a different mathematical morphology method was used, namely the watershed (Beucher and Lantuéj 1979) algorithm. This method aims to detect local maxima positions in a given grayscale image. The intuition behind the method is the following: the method considers the image topology to be a succession of peaks and valleys; in the bottom of the valleys, it is assumed to exist holes. If a liquid would enter the valleys through these holes, at the same time for holes at the same depth, there would be an instant when the liquids in two consecutive valleys would merge. The position where those liquids merge is considered to be a local maximum, as depicted in Fig. 8.

The loci of the maxima can be used to detect the center of each one of the dark fringes. To do so, one initially needs to obtain the complement of the image, therefore making each peak a valley and each valley a peak. After that, one
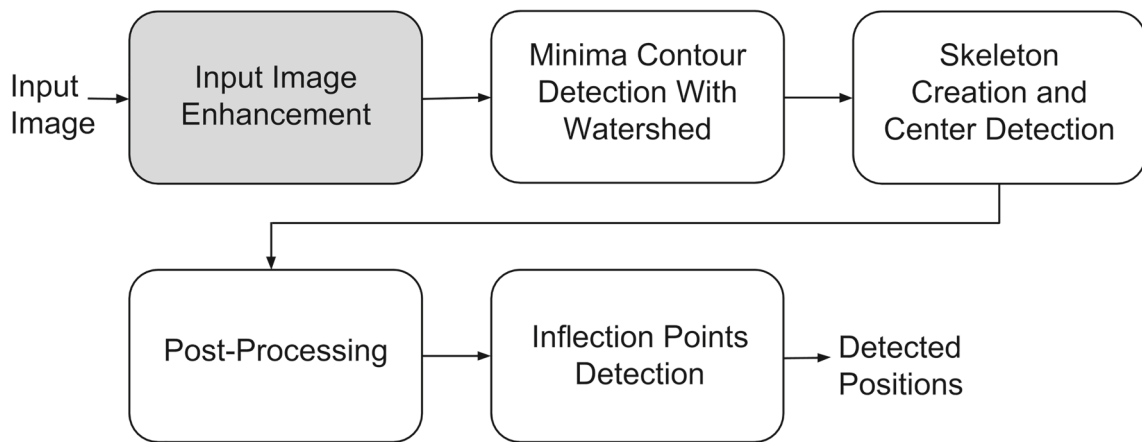
Fig. 4 Input image enhancement

Fig. 5 Highlight of the gaps of the fringes connecting consecutive dark and bright fringes. The dark regions have lower pixel values, whereas the bright regions have higher pixel values
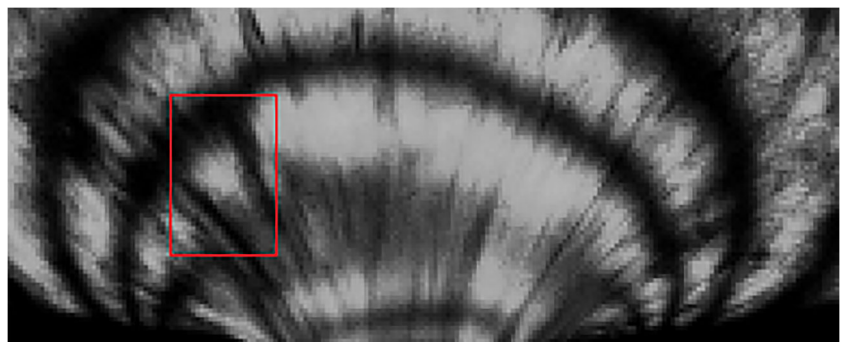

Fig. 6 Example of birefringence images before and after the enhancement step based on the white top-hat and black top-hat operations. Its effect is best observed at the consecutive bright and dark fringes in the modified image: **a** original image; **b** enhanced image with increased contrast. **c** Detail of the original image. **d** Detail of the enhanced image. The contrast between the fringes and the background is greatly enhanced in panel (**d**) in comparison to panel (**c**); it can be better observed in the electronic version of these figures

(a)

(b)

(c)

(d)
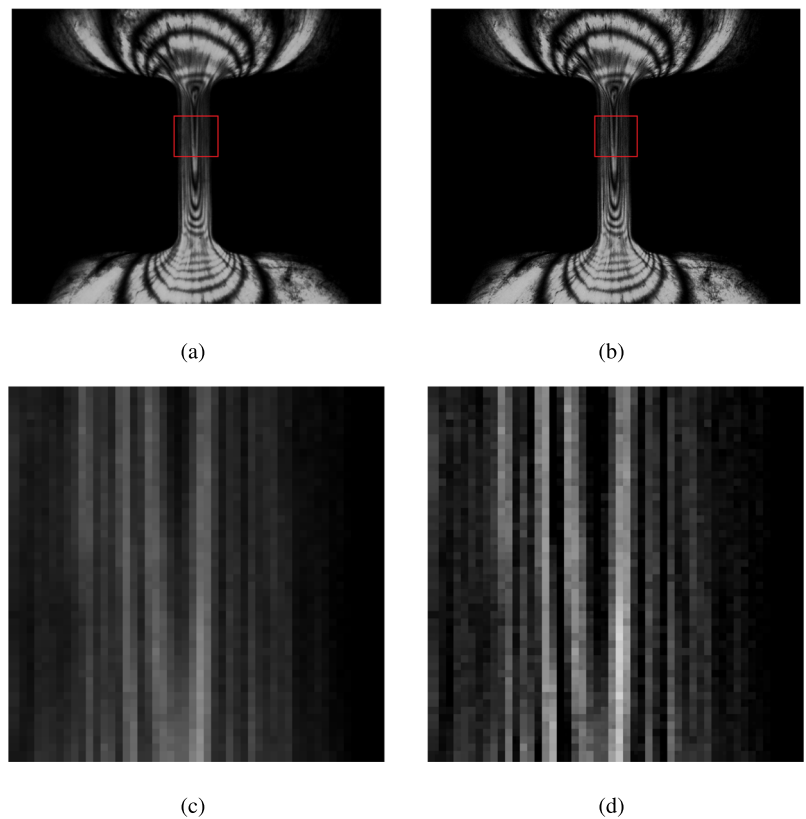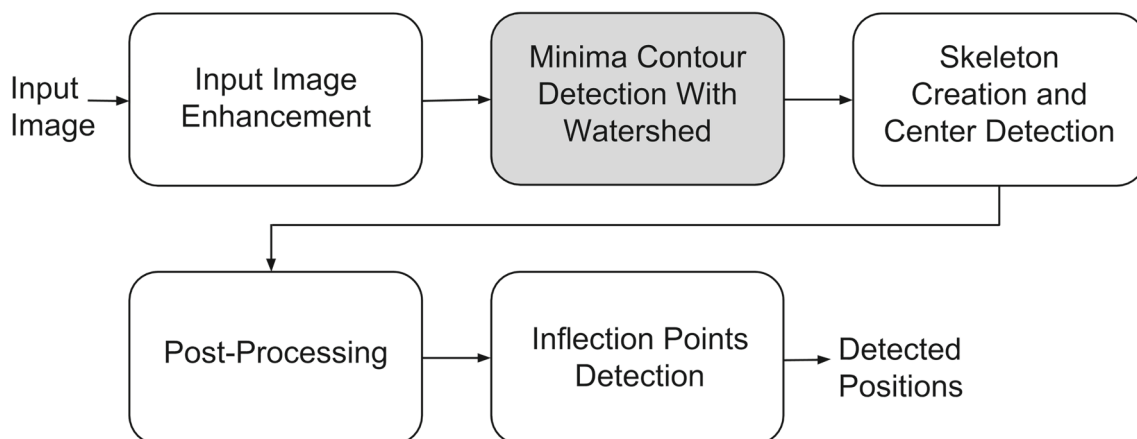
Fig. 7 Minima contour detection with watershed

should apply the watershed method to the inverted image. An example of the result, obtained with this procedure, can be seen in Fig. 9a, where the resulting analysis still present some detection artifacts.

Although this result seems to be initially encouraging, one can readily see that it is not enough to solve the problem of detecting the position of the dark fringes, as this simple application of the watershed method creates an image with

Fig. 8 Watershed peak detection method. The inner peaks are detected and marked as the red vertical lines

(a)   (b)
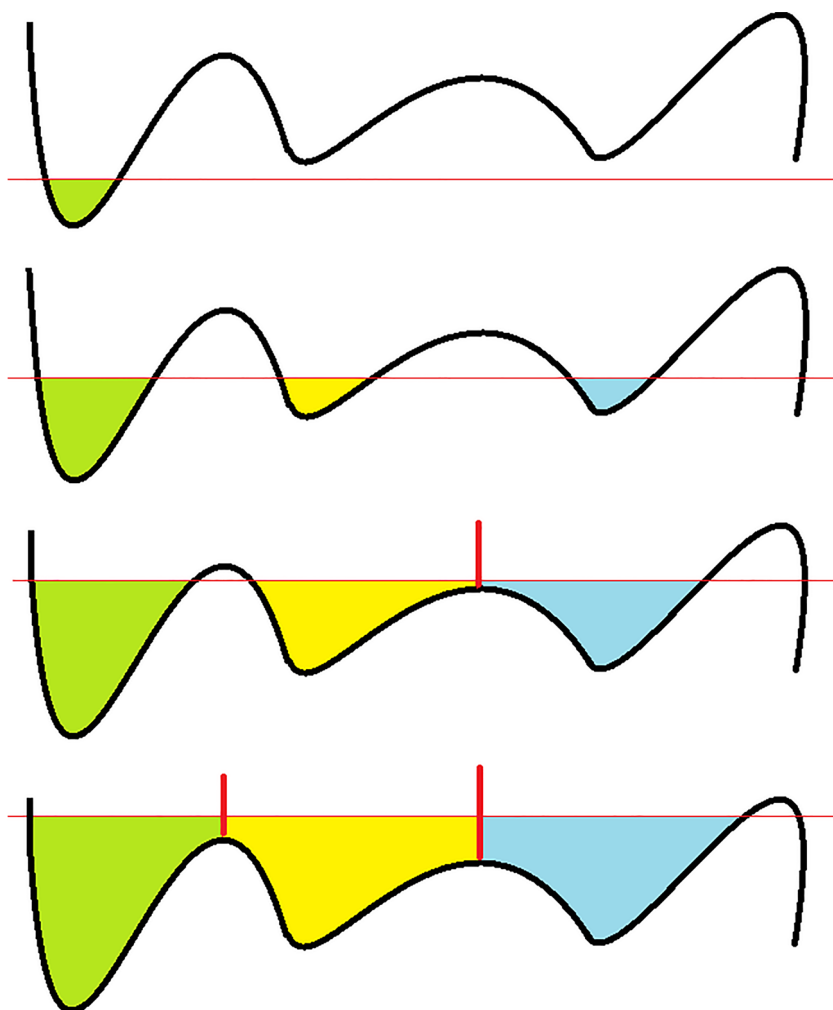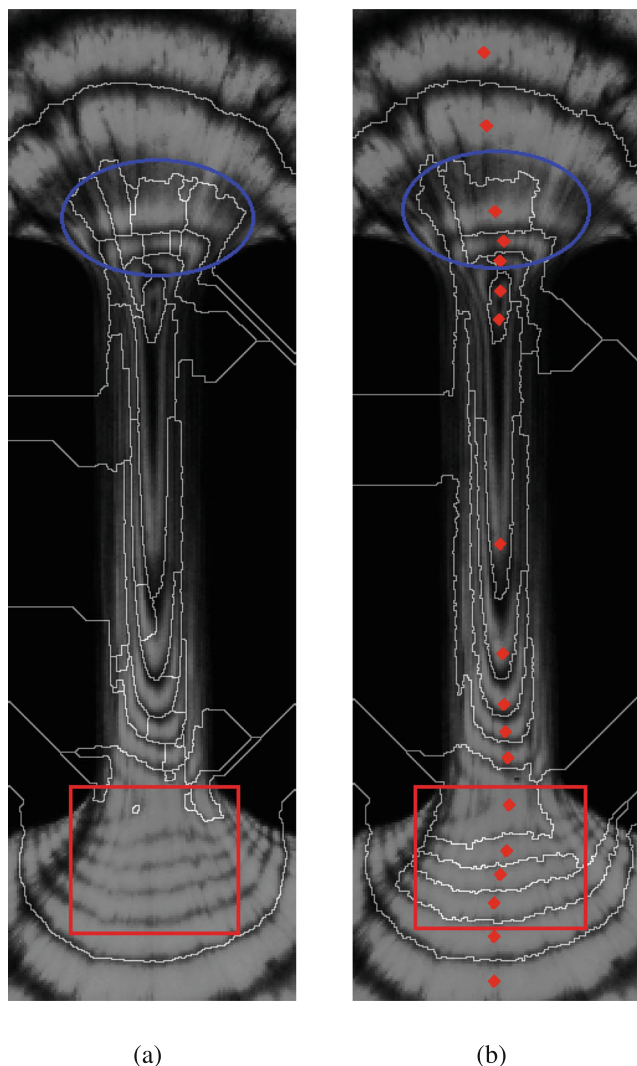
Fig. 9 Contours of the dark fringes obtained with the use of the watershed method. **a** Without minima imposition. **b** With initial minima imposition (marked as a red diamond). The blue ellipses and the red rectangles show, respectively, regions where there is over-segmentation and undetected fringes in the version without minima imposition

under- and over-segmentation, both missing boundaries or displaying undesired boundaries. This can be improved by feeding the algorithm with some prior knowledge, like the approximate positions of the maxima (or minima). In our proposed approach, a human user must input the location of every bright fringe (the minima points in a inverted image). The imposition of those minima locations (Soille 2003) creates a mask f_m whose values are t_{max} (the maximum value allowed to the pixel) except where the minima were imposed (where the mask value is set to 0), as given by the following:

$$M = \begin{cases} 0, & \text{if a minimum was imposed} \\ t_{max}, & \text{otherwise} \end{cases}, \qquad (10)$$

where t_{max} is the largest possible pixel value in the grayscale image. This process is detailed in Fig. 10.

We then take the minimum between each pixel value and the value of the mask in that position, whose result is called $(f + 1) \wedge f_m$ in Fig. 10b. After that, the signal f_m is considered the marker and the signal $(f + 1) \wedge f_m$ the mask of a geodesic erosion, as defined in "Geodesic morphology." Successive geodesic erosions are performed (Fig. 10c–g) until the image becomes unchanged by further erosions (Fig. 10h). Note that, when you perform the minima imposition, the imposed minima will be the only local minima in the resulting image, lending to it a smooth appearance.

After the minima imposition, we then apply the previously described watershed method to the resulting image to obtain the maxima contours, avoiding in this case under- and over-segmentation issues. An example of the results after the minima imposition can be seen in Fig. 9b, which improves upon the results shown in Fig. 9a. One can see in the region highlighted by a blue ellipse that the minima imposition technique reduces some over-segmentation artifacts while, as seen in the region delimited by the red rectangle, and also increases the amount of successfully detected fringe contours.

Skeleton creation and center detection

After we obtain the minima contour with the watershed operation, we need to further process it in order to produce 1 pixel-wide contours. To do so, we employ the skeletonisation technique described in this section.

The result of the watershed method is a binary image that indicates boundaries that separate each bright region, so it should represent a centerline for the dark fringes. In order to select the exact position of the fringe centers, it is necessary that the contour lines are exactly one pixel wide. Sometimes, after using the watershed method, the contour lines are thicker than one pixel, thus lowering the accuracy of the method. To deal with this problem, we propose (Fig. 11) the use of a skeletonisation method (Haralick and Shapiro 1992). A morphological skeleton of a binary image such as the contours in Fig. 9 is defined as the locus of the center of the maximal disks completely contained in the image. Figure 12 shows the step-by-step procedure to obtain the skeleton of an image. This procedure creates thinner segments with a thickness of one pixel, which is mandatory for the next steps.

Post-processing

After obtaining the pixel-thin contours, we proceed to the estimation of the fringe center position, as well as removing the false detections. This section describes the post-processing methods (Figs. 13 and 14) employed in this task.

Fig. 10 Minima imposition method. **a** Original figure f and mask f_m. The pixel values for a section of image are represented as gray bars, and the values of the mask are given by the solid black lines. **b** Pixel-wise minimum between f_m and $(f + 1)$, which is defined as $(f + 1) \wedge f_m$. **c** Morphological erosion of f_m. **d** Maximum between $(f + 1) \wedge f_m$ and the result of the morphological erosion of f_m. The red-dashed line shows the values that were changed in the maximum operation. **e** The final result of the first geodesic erosion of f_m is represented by the values in solid black lines. **f** Second geodesic erosion of f_m. **g** Third geodesic erosion of f_m. **h** Fourth geodesic erosion of f_m. The signal remains unchanged after any other geodesic erosion, so it is considered the reconstruction via successive erosions of $(f + 1) \wedge f_m$ from the mask f_m

(a)

(b)

(c)

(d)

(e)

(f)

(g)

(h)
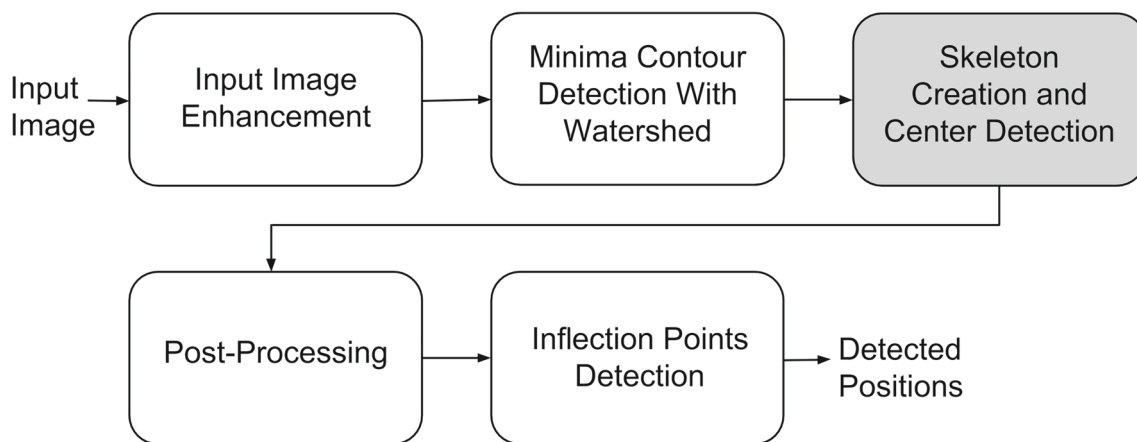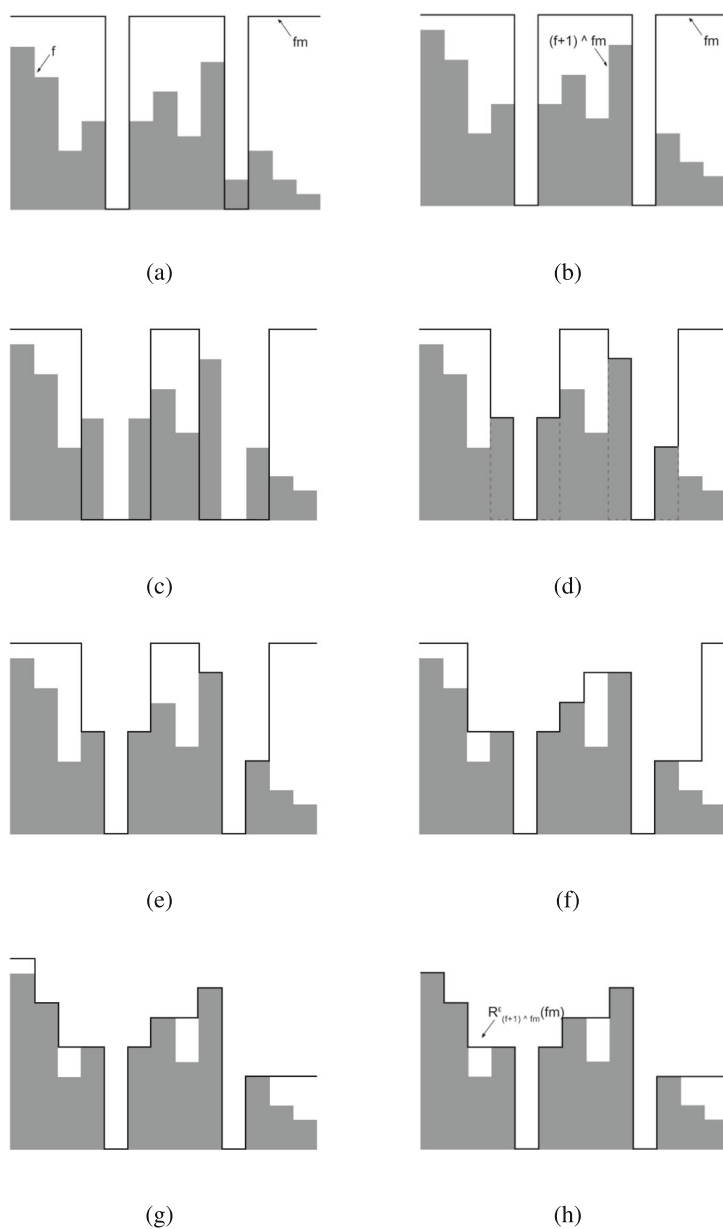
Fig. 11 Skeleton creation and center detection

Fig. 12 Skeletonisation using maximal disks. The union of all maximal disk centers defines the skeleton. **a** Original image. **b** Some maximal disks and the initial construction of the skeleton. **c** Maximal disks covering the whole image. **d** Complete skeleton
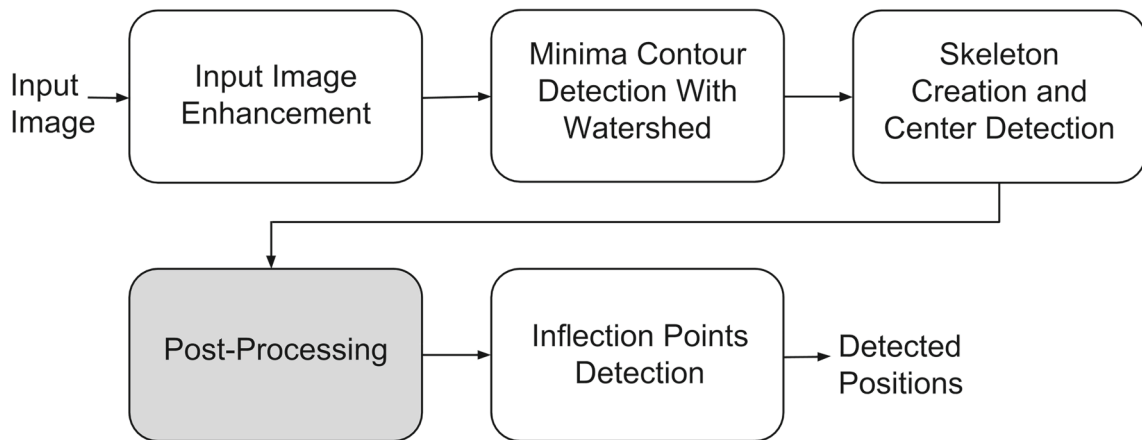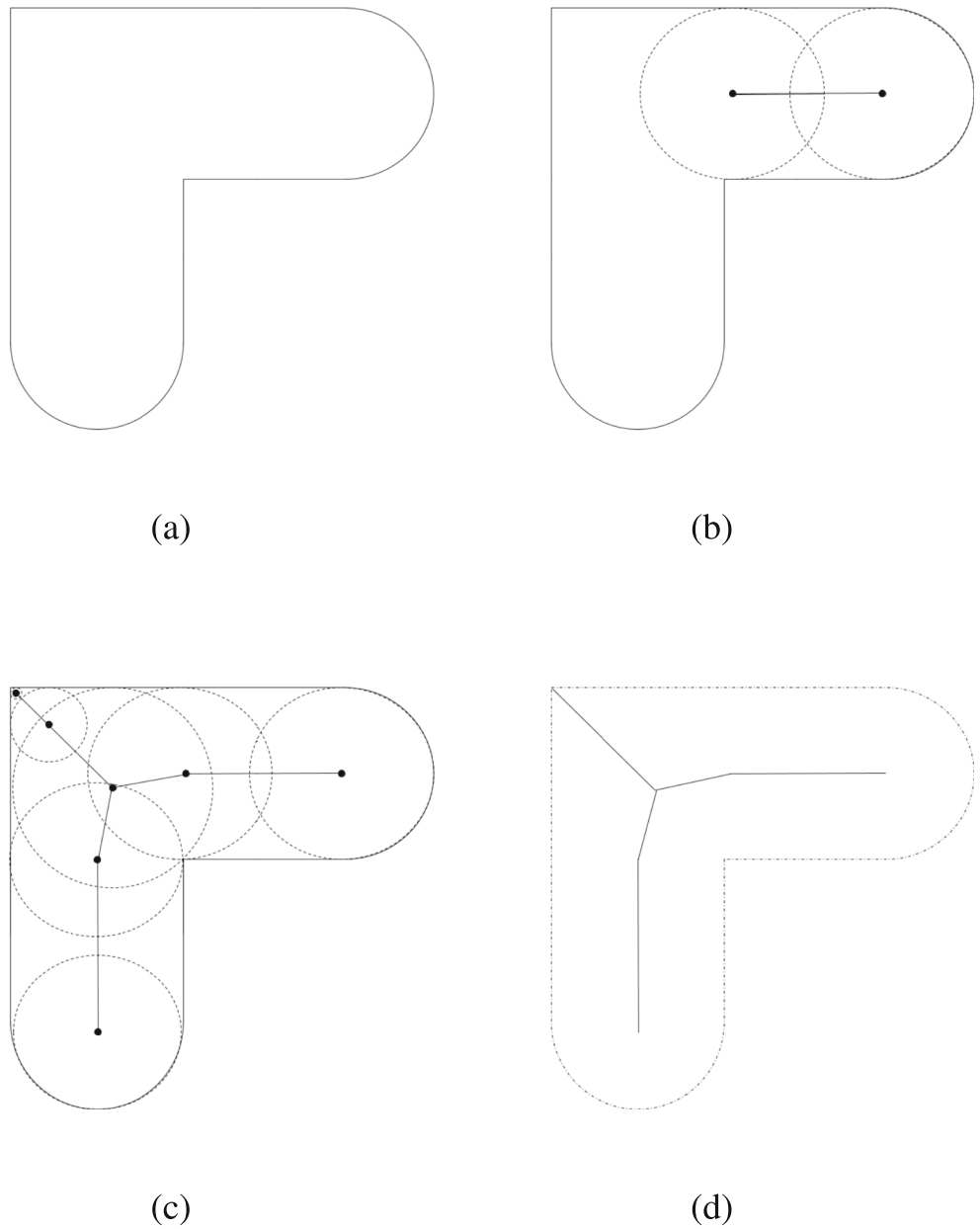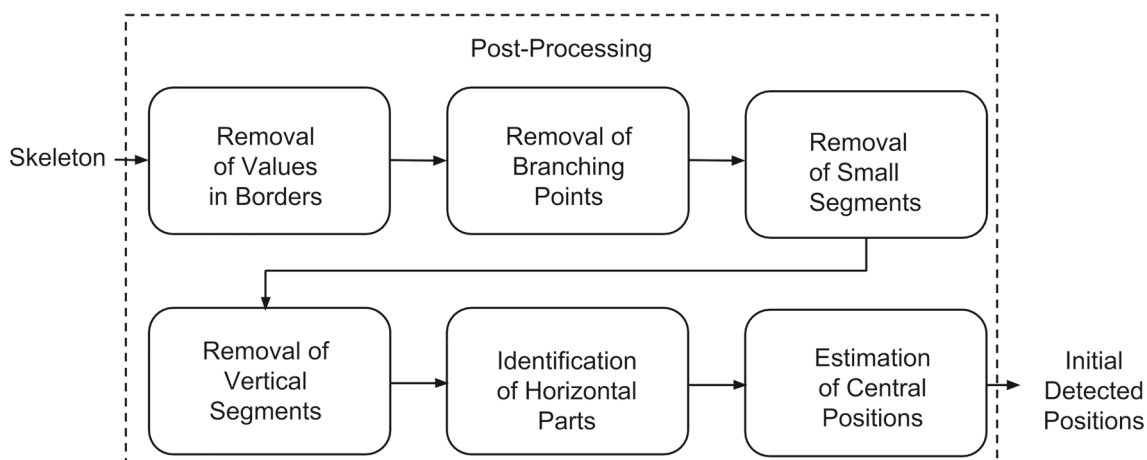

(a)

(b)

(c)

(d)

Fig. 13 Post-processing

Fig. 14 Detailed block diagram of the post-processing

At this point, the contour lines, which we expect to be present only in the dark fringes, may also erroneously appear in a bright fringe. As can be seen from Fig. 15, the contours have some segments that do not belong to the dark fringes and should not be used to estimate their position. This figure also shows that those segments have a shape similar to a vertical line, being perpendicular to the fringe variation. The algorithm uses this fact to detect and remove flaws in the contours by separating it in small segments and removing those that have a vertical orientation. In addition, one is not interested in identifying the whole dark fringe but only the position of its center; therefore, the contours can
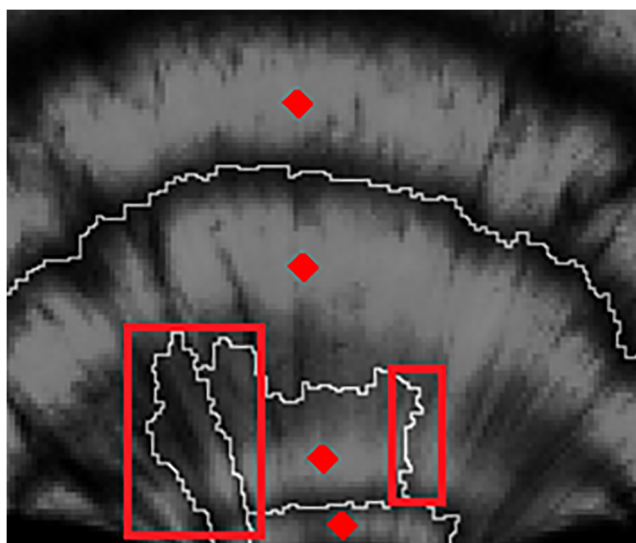
be further processed in order to extract only the required information. The post-processing pipeline is depicted in Figs. 13 and 14 and is described in the next sections.

Removal of values in borders

In the first step, only the center columns of the image are kept, which contain the region of interest for the detection of the fringe positions.
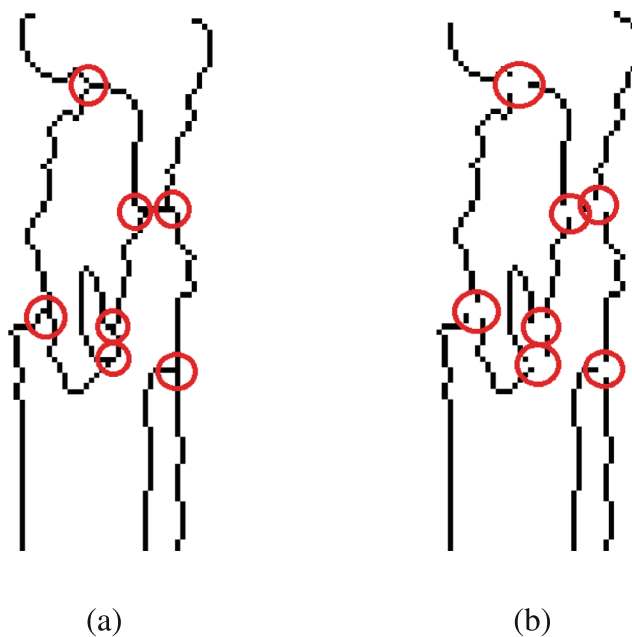

Fig. 15 Detail of the contours of the dark fringes obtained with the use of the watershed method showing some flaws in the detection, with parts of the contour highlighted by a red square appearing in the bright fringe

Fig. 16 Detail of the branching points removal method, where the circles show the points to be removed. The branching points are considered as the points connected to three or more points. **a** Before branching point removal; **b** after branching point removal

Removal of branching points

At this point, we only want to detect the center of the dark fringes, which in our database are horizontally oriented and often elongated in the images. Therefore, we can split the detected skeleton in smaller segments in order to detect the segments that are also horizontal and elongated (and thus likely to belong to the desired dark fringes).

The branching points, which are points connected to three or more points, are removed from the remaining skeleton that, after this operation, will be just a set of unconnected segments, as seen in Fig. 16. It is important to notice that the branching point removal step applies only to the fringes skeleton (as can be seen in Fig. 16), and not to the actual fringes. Thus, this process do not affect the geometry of the fringes if they present ramifications.

Removal of small segments

After this step, several spurious segments may still remain. Since it is expected that the dark fringes are horizontal and elongated in the region of interest, we count for each segment the number of points contained in it, and the segments that have less than a given number of points are removed from the structure.

Removal of vertical segments

For the same motivation as in the previous step, we also analyze each segment and measure its horizontal length. This is done by counting the number of columns that it occupies, removing those that have a horizontal length smaller than a threshold (in other words, are "too vertical"). This is done because they, most likely, do not correspond to the desired center position of the fringes. An example of segments that remain after these cleaning steps can be seen in Fig. 17.

It is important to notice that, for different sets of images, such fringes may present different orientations, due to different geometries of the experiments. For example, if such fringes happen to be mainly vertical, this procedure can be adapted by removing instead the horizontal segments.

Identification of horizontal parts

In this step, we want to determine the vertical position for the center of each dark fringe. Comparing Figs. 9 and 17, one can see that due to the shape of the dark fringes the remaining segments have a parabolic shape with a vertical orientation, whose peak indicates the position of the center of the fringe. Therefore, in order to identify this center, we detect the peaks in the segments by using a
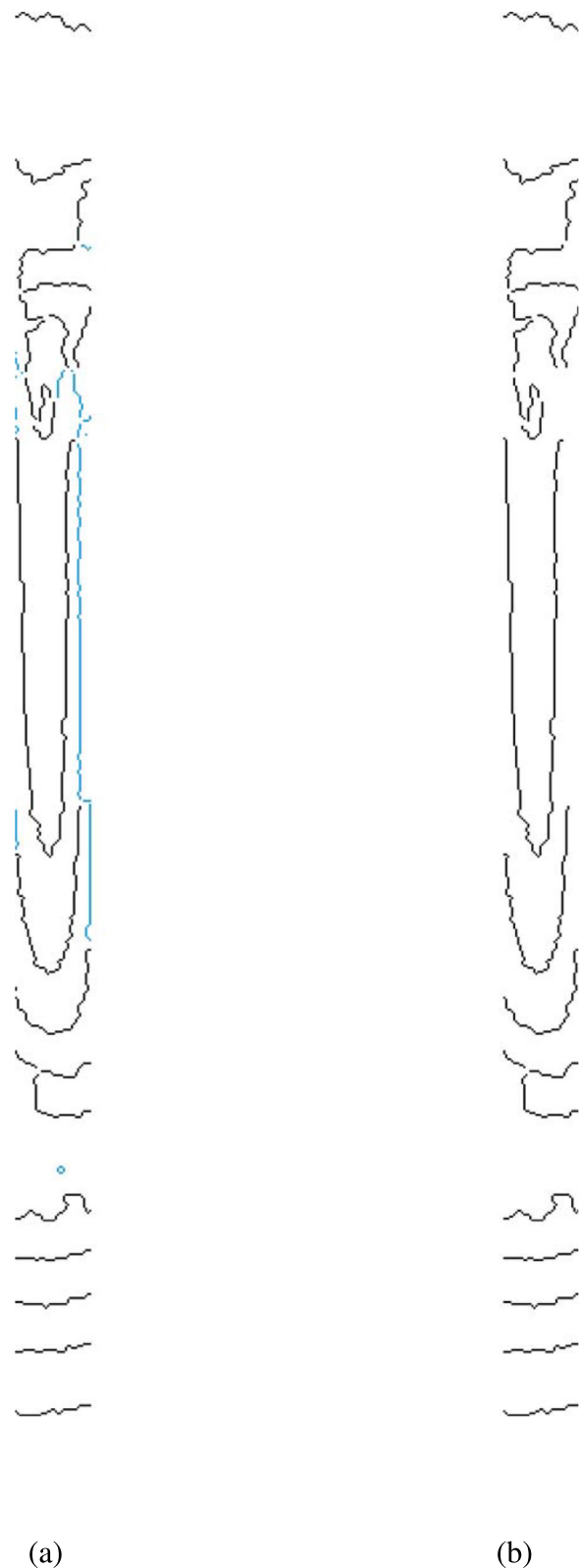

(a)   (b)

Fig. 17 Final selection of the segments after the spurious segments are removed: **a** before segment removal; **b** after segment removal. The removed spurious segments are marked as light blue in the figure. This figure can be better understood when observed on a screen
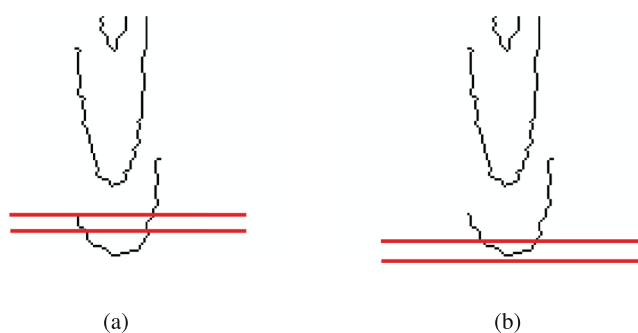
Fig. 18 Selection of the horizontal part of the segments. **a** Wrong region—few points. **b** Correct region—largest number of points

horizontal window to select for each segment the part that has the largest number of horizontal points. As illustrated in Fig. 18, when sliding the horizontal window along the vertical direction, the position that yields the largest segment corresponds to the location of the peak (within a certain accuracy given by the window width).

Estimation of central positions

Finally, the center position of each fringe is selected as the mean of the vertical coordinates of each skeleton pixel within the horizontal window. If after this step more than one center position is detected between two consecutive maximal points manually input, only the one with the greater number of points is kept. This step is illustrated in Fig. 19a, and the final result is shown in Fig. 19b.

Inflection points detection

After selecting the correct segments to represent each fringe, we proceed to the detection of the inflection point of the image. This section describes the employed procedure.

A final important point for the characterization of the flow is an inflection point (Fig. 20). As reported by Castro et al. (2018), this point helps to characterize the geometry of the experiment and is defined with the maximum retardation order in the flow, despite not being associated to the horizontal part of any dark or bright fringe in the images, as one can see in Fig. 21. In order to estimate this point, the algorithm described in "Input image enhancement"– "Post-processing" is applied in the transposed images to detect the two vertical dark fringes around the inflection point , and its position is defined as the average of the center of the two vertical fringes. An example of this detection is show in Fig. 22.
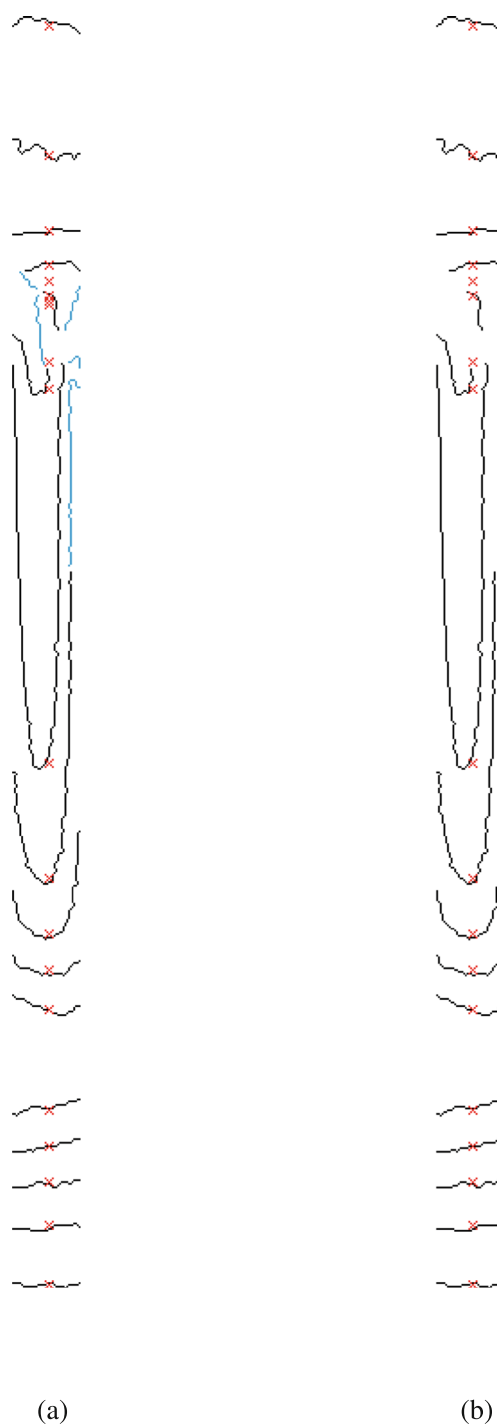
Fig. 19 Detected positions for each segment. The red X marks in the center column the vertical coordinates for the segment that has the largest number of horizontal points, which represents the center for each dark fringe according to the procedure described in "Estimation of central positions." **a** Result before the elimination of double detections. **b** Final result, after the elimination of double detections. The ambiguous segments, marked as light blue, were also removed. This figure can be better understood when observed on a screen
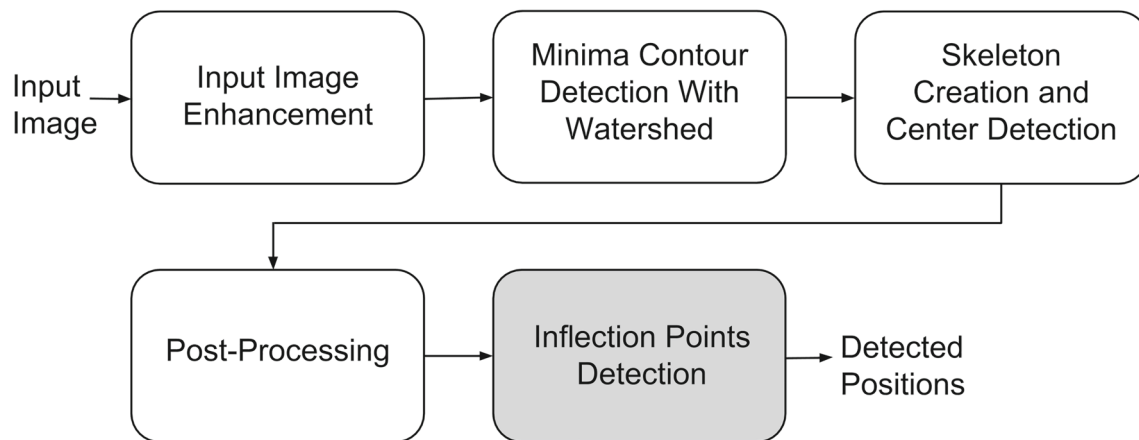
Fig. 20 Inflection points detection

Comparison with other fringe center detection methods

In this section, we will analyze the algorithm performance, starting from a description of the experimental framework, followed by a performance assessment to calibrate the algorithm. The results of the proposed algorithm are first compared to other methods found in the literature and then compared to the reference method.

Experimental framework

The algorithm described in "Processing of birefringence images using mathematical morphology techniques" was developed in MATLAB© (MATLAB 2012) environment using morphological function implementations present on the Image Processing Toolbox. The results were obtained

using a computer with a Xeon E3-1270 v5 3.6GHz processor and 32GB of RAM.

The flow-induced birefringence images acquired during a steady state for two polystyrene samples were presented in Castro et al. (2018), as was also the determination of fringes order (k). Images of flow-induced birefringence analyzed in this work were obtained from a previous work by Farias et al. (2014), using two samples of polystyrene, GPPS1 (Mw = 180000 g/mol) and GPPS2 (Mw = 280000 g/mol), in the multipass rheometer (MPR4) available at the University of Cambridge, Department of Chemical Engineering and Biotechnology (UK). The single-pass operation mode was used, which consists of moving both pistons up or down at a single speed, which forces the material to flow through the slit die. The slit die
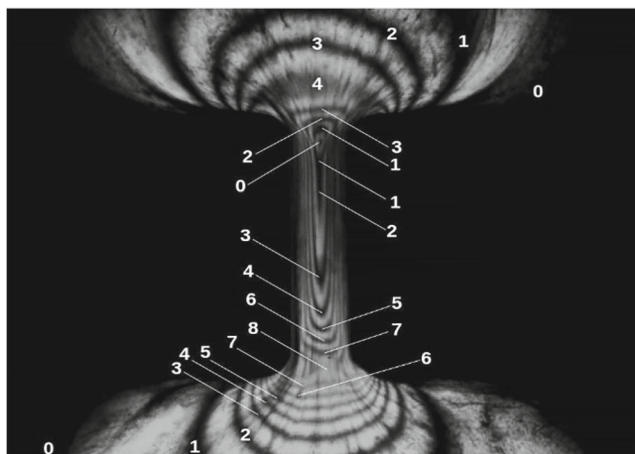

Fig. 21 Fringe retardation order (k) of sample GPPS1 at 1 mm/s. The inflection point is reported by Castro et al. (2018) as the one with a retardation order $k = 8$ and is related to the geometry of the experiment

Fig. 22 Example of the detection of the inflection point. The center of the white contours associated to each vertical fringe is marked as a cross and the estimated inflection point is marked as a circle

Fig. 23 Configuration of the MPR with the birefringence setup and schematic outline of slit-die. The polymer flows upwards along the centerline represented by the red dashed line
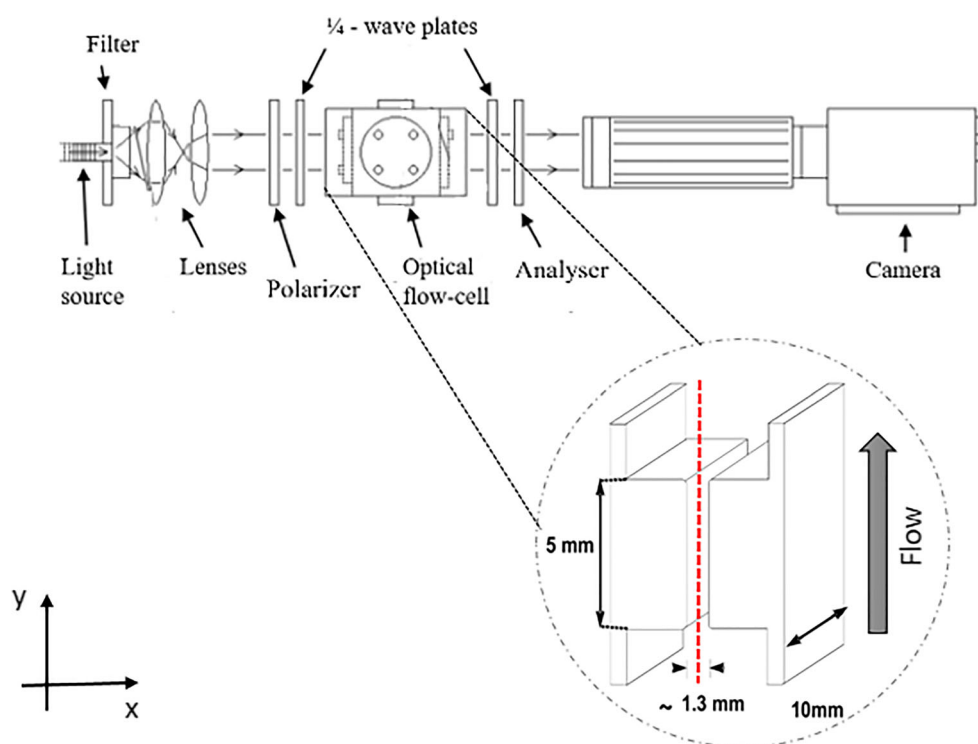
geometry used in the experiments has a 5-mm length and 1.3-mm width. The width is very small in order to limit the side effects on the glass. The flow direction through the slit was upward at different velocities (0.5; 1 and 2 mm/s in the experiments using GPPS1 sample and 0.2; 0.5 and 1 mm/s in the experiments using GPPS2 sample).

Optical birefringence set up (light source and monochromatic filter, polarizer, quarter wave plates, analyzer and camera) and schematic outline of slit die geometry are shown in Fig. 23.

It is important to note that the algorithm proposed here is not entirely automatic because it requires that, for each different experiment, an operator inputs a point in any position inside each bright fringe. The set of point thus generated, which is shown as the red diamonds in the

example of Fig. 28b, is used for the minima imposition operation described in "Minima contour detection with watershed." In the results that follow, a set of input points was defined for each experiment and used for all images of the same experiment.

Performance assessment

In this section, the proposed algorithm is thoroughly analyzed. In the first experiment, the pre-processing step described in "Input image enhancement," which includes image enhancement and minima imposition, is enabled and disabled to show its effectiveness. Then, two parameters present in "Post-processing" have their value adjusted, namely the threshold that controls the removal of spurious

Fig. 24 Mean square error (mm^2) for several values of the window width. **a** Without pre-processing. **b** With pre-processing
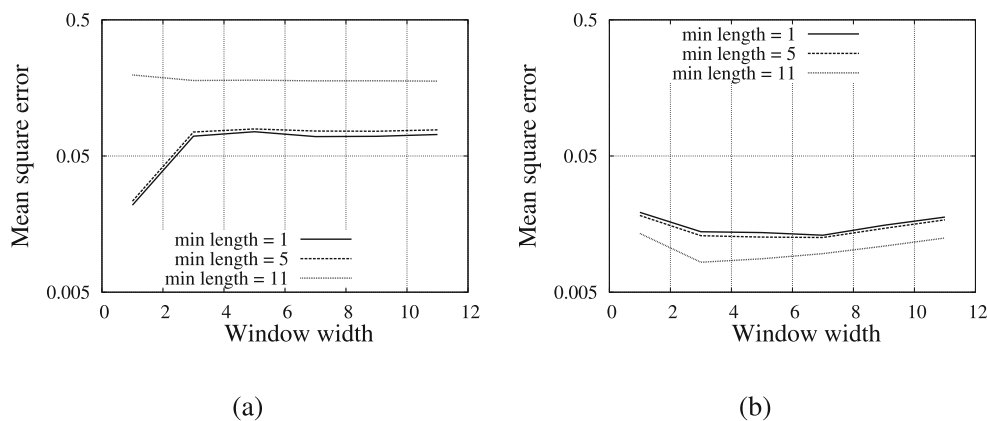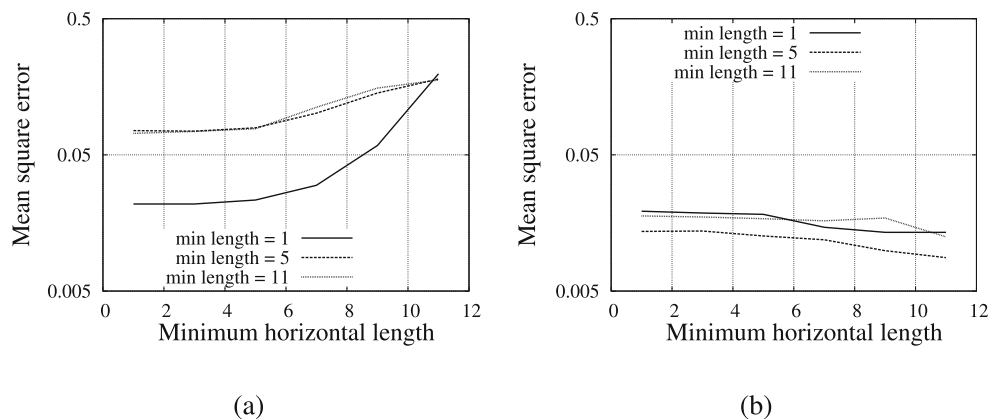

(a)

(b)

Fig. 25 Mean square error (mm^2) for several values of the minimum length threshold. **a** Without pre-processing. **b** With pre-processing

(a)

(b)

elements (see Fig. 17) and the width of the window that selects the horizontal part for each segment, which represents the center of each dark fringes (see Fig. 18).

In order to define an objective evaluation, the measurements obtained by Castro et al. (2018) were considered as a ground truth, and for each algorithm setup, the mean square error between the obtained fringe positions and the ground truth was computed. For this evaluation, only the experiment obtained with the GPPS1 flow at 1 mm/s was used, since it shows a pattern where the fringes are neither too few nor too thin.

Determination of the fringe center

As described in "Identification of horizontal parts," the detected contours have a shape similar to a noisy parabola positioned inside the dark fringes, and the center of each dark fringe is identified by the vertex of this parabola. A simple way that has been devised to find the position of the vertex is to use a moving horizontal window, analyzing for each position the part of the contour that fits entirely inside this window and identifying the one with the largest length. In order to do so, we must define the optimal width of the horizontal window. A window that is too thin may

lead to a false detection due to noise. If it is too wide, the algorithm is able compensate the noise but it loses precision. In this experiment, we analyze different window widths and determine the one that provides the lowest average error for the algorithm.

Figure 24 shows an evolution of the mean squared error obtained by the algorithm for several values of the window width. In the figure, the multiple curves represent the results for a fixed value of the other parameter, the length that separates spurious, and accepted elements. In Fig. 24a, the pre-processing is disabled while in Fig. 24b it is enabled. It is important to notice the range of the error values, since in the curves with the pre-processing disabled, the minimum observed error is higher than the maximum error with the pre-processing enabled. Comparing only the best results for each case, the pre-processing step reduces by up to 20 times the error in the proposed algorithm.

In Fig. 24b, the curves reveal the two cases where the error tends to be higher: if the window is too restrict, so it is more likely to contain small peaks in the data, and too big, so the window contains larger segments that may not represent the fringe centers. There seems to be a region for some intermediate values where the error reaches its minimum and is less sensitive to the variation of this

Fig. 26 Detection rate for several values of the minimum length threshold. **a** Without pre-processing. **b** With pre-processing

(a)

(b)
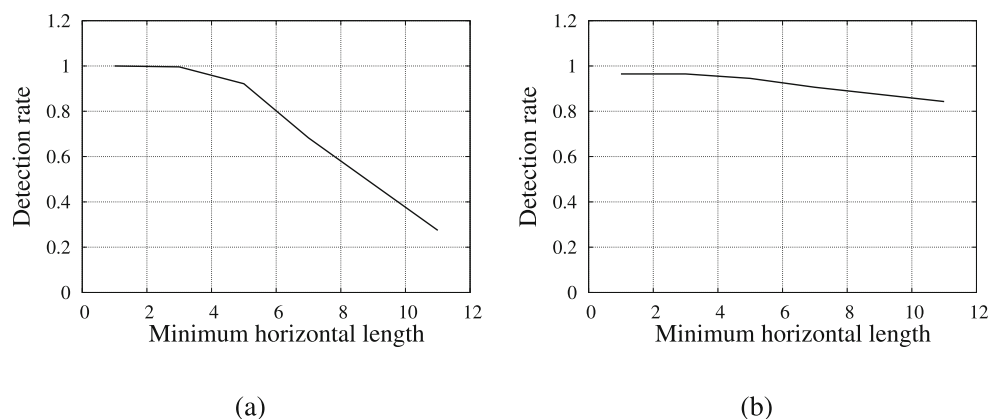
parameter. To determine a compromise in the algorithm configuration, the window was defined to have a width of 5 pixels.

Removal of spurious elements

In the detected contours, part of the noise is due to impurities in the experiments, which create undesirable contours inside the bright fringes. As described in "Removal of vertical segments," a post-processing step separates the contours in segments and removes from the final detection the ones with a length smaller than a threshold. There is an optimum value for this threshold. If it is too big, it is possible that all segments associated to a fringe are removed and no position estimate can be provided. In this experiment, we evaluate the impact of the threshold that removes undesirable segments in the detection of the fringe centers.

In Fig. 25, one can see the relation between the mean square error and the minimum segment length for a few fixed values of the window width. Another important aspect in this experiment is the detection rate, that is, the amount of fringes where there is at least one detected segment and the algorithm can estimate a fringe center. This characteristic is exemplified in Fig. 26.

Comparing Figs. 25a and 26a, one can see that the error increases with a bigger threshold. This behavior can be explained by the fact that without the pre-processing step, the algorithm creates spurious segments that are indistinguishable from the true segments (the ones that follow the fringe pattern), so any attempt to remove wrong segments also removes the true ones, and the detection rate drastically falls when the threshold is increased. With the inclusion of the pre-processing step, a different behavior can be seen, as shown in Figs. 25b and 26b. With bigger values

for the acceptable segment length, more spurious segments are removed while still keeping an amount of accepted segments, since the detection rate shows a smaller decrease, and the mean square error is in fact reduced. In order to provide an algorithm able to detect the fringe positions for at least 95% of the cases with the smallest error, the threshold value was defined as 5 pixels.

Comparison with other methods

Two other methods were evaluated in comparison with the proposed method. Those methods were developed to detect fringes on images originated in different experiments and were adapted to context of birefringence images.

The method of Farooq et al. (2015) separates the bright and dark fringes by binarizing the images using a threshold that can be constant or adaptive, and then applies a skeletonisation technique to find the central position for each fringe. Due to impurities in the experiments, the image has a cracked appearance. A simple constant threshold is not able to distinguish every bright and dark fringe in the images, as can be seen in Fig. 27a. However, by manually selecting two levels of threshold to be used in different parts of the image, a good compromise between algorithm performance and model overfitting can be found, as shown in Fig. 27b.

The works of Yu and Andresen (1994) and Zhang et al. (2002) described a technique to detect fringes in light interferometric experiments. First, it estimates a local orientation map for each pixel (Yu et al. 1994), and pre-processes the images by applying a directional median filtering that uses the estimated orientation in order to remove the noise tangent to fringe orientations while also keeping sharp transitions perpendicular to the fringe orientations. Afterwards, the method computes the

Fig. 27 Birefringence image binarization. **a** With a constant threshold. **b** With two levels of threshold

(a)

(b)

Fig. 28 Contours of the dark fringes obtained with: **a** Farooq et al. (2015) and **b** Yu and Andresen (1994) and Zhang et al. (2002)

(a)   (b)
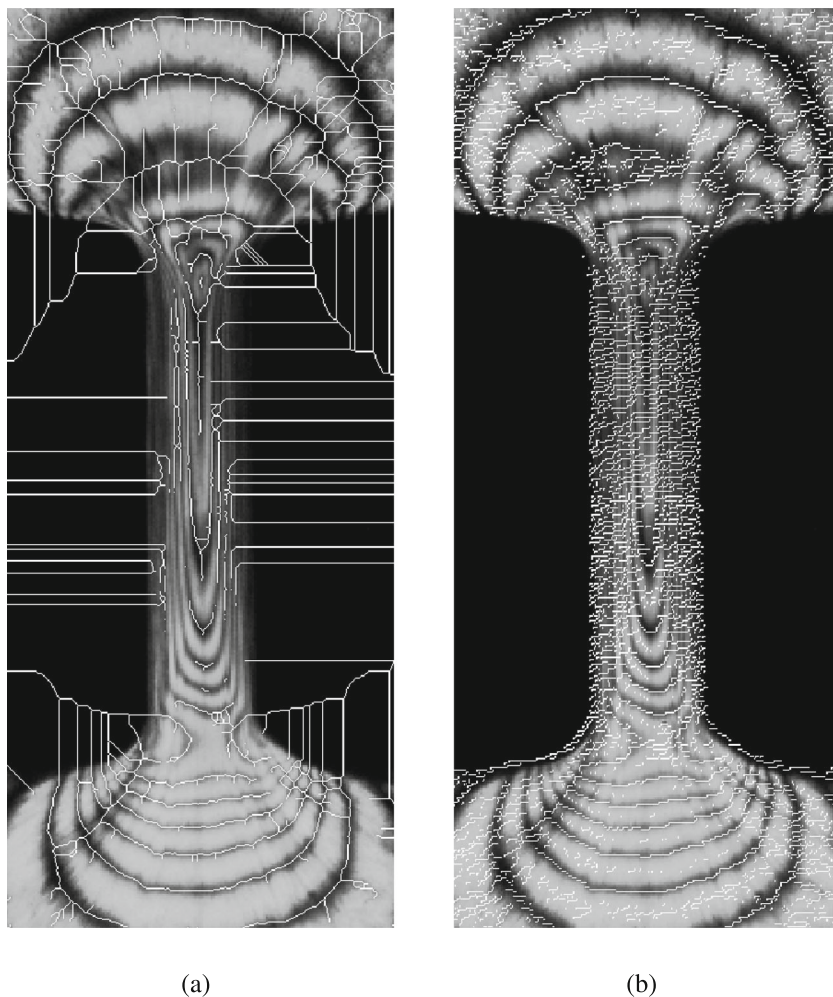
directional derivatives of the pre-processed images, also using the orientation map. Then, it binarizes the directional derivatives and considers the fringe centers as the edges of this binarized image, that is, the positions where there is a fast transition between a positive and a negative gradient.

However, also due to the characteristics of the birefringence images, the estimation of an orientation map is likely to produce a noisy result, so instead, this implementation uses only a horizontal median filtering, since it corresponds to the expected orientation of the fringes in the center of the images, which is the region of interest

for the detection, and computes only the vertical derivative to be used in the binarization and detection step. An example of the implementation of the methods in Farooq et al. (2015) and Yu and Andresen (1994) and Zhang et al. (2002) applied to the birefringence images can be seen in Fig. 28.

The same objective evaluation used to setup and validate the algorithm is employed in the comparison with the aforementioned methods. Since those methods only provide a basic skeleton of the fringe image, no precise central position is extracted. In order to properly

Table 1 Mean square error (mm^2) obtained with the proposed method, the method based on the image derivative (Yu and Andresen 1994; Zhang et al. 2002) and the method based on image binarization (Farooq et al. 2015)

Pre-processing	Proposed	Derivative	Binarization
No	0.086	0.029	0.019
Yes	0.013	0.043	0.019

Table 2 Detection rate obtained with the proposed method, the method based on the image derivative (Yu and Andresen 1994; Zhang et al. 2002) and the method based on image binarization (Farooq et al. 2015)

Pre-processing	Proposed	Derivative	Binarization
No	0.85	1.00	0.93
Yes	0.95	1.00	0.93

compare with the proposed method, the post-processing step described in "Post-processing" and optimized in "Performance assessment" is also applied.

In Table 1, one can see a comparison of the mean squared error obtained with each method. For the method of Farooq et al. (2015), no pre-processing step is defined, so in order to provide a fair comparison the proposed pre-processing was also tested with this method. The works of Yu and Andresen (1994) and of Zhang et al. (2002) already include a median filtering to enhance the image, and for this reason, two cases were considered. In the first one, the algorithm was tested using only the median filter, which is labeled as no pre-processing in Table 1. In the second one, the algorithm was tested with the median filter in addition to the presently proposed pre-processing, which is labeled as with pre-processing in Table 1.

Table 2 shows the detection rate for the same methods and configuration. Comparing the performance of the mean square error and the detection rate, one can see that the proposed method, with the correct configuration, produces a result with the lowest error while providing the second-best detection rate, being better than the binarization method in both metrics. In addition, while it produces a detection rate lower than the one of the derivative method, its mean squared error is twice as small. In addition, one can also see from the results in Table 1 that the works of Yu and Andresen (1994) and Zhang et al. (2002) have a loss of performance in the presence of the pre-processing step. The reason for this behavior is that, as a by-product of the minima imposition technique, the resulting image loses its original local minima, presenting only the imposed minima, as discussed in "Minima contour detection with watershed."

Fig. 29 |PSD| as a function of distance along the centerline depicted as the red-dashed line in Fig. 23. **a** GPPS1 flow at 0.5 mm/s. **b** GPPS1 flow at 1 mm/s. **c** GPPS1 flow at 2 mm/s. **d** GPPS2 flow at 0.2 mm/s. **e** GPPS2 flow at 0.5 mm/s. **f** GPPS2 flow at 1 mm/s
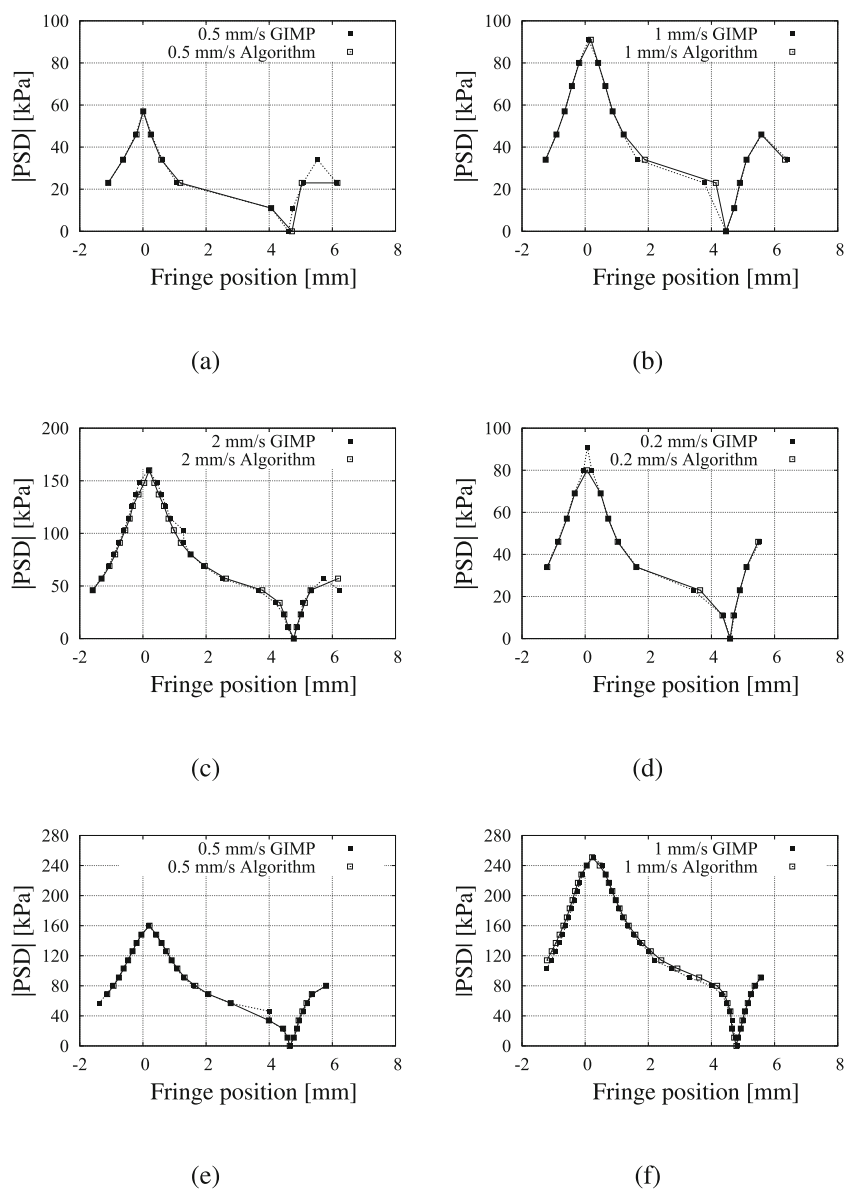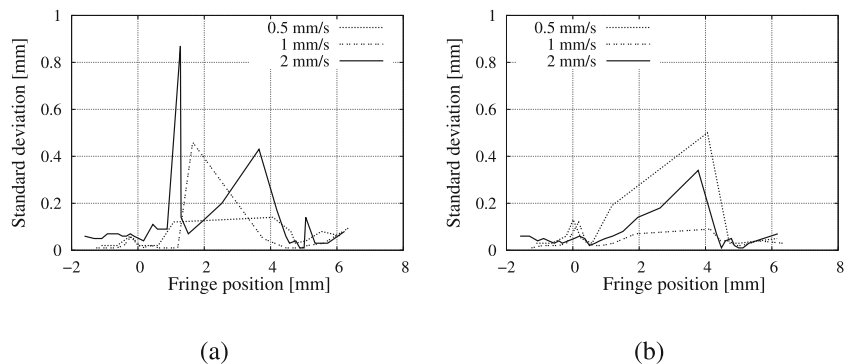
Fig. 30 Standard deviation S as a function of distance along the centerline for the sample GPPS1. The centerline is depicted as the red-dashed line in Fig. 23. **a** Manual method (GIMP). **b** Proposed morphological approach

(a)

(b)

Comparative evaluation with reference method GIMP

The results obtained using the approach presented in "Processing of birefringence images using mathematical morphology techniques" after processing 15 images for each experiment were compared with those disclosed in Castro et al. (2018), in which a semi-automatic methodology based on the GIMP software was proposed. For this purpose, we chose to consider the flow direction through the slit at three different velocities (0.5, 1, and 2 mm/s in the experiments using GPPS1 sample and 0.2, 0.5, and 1 mm/s in the experiments using GPPS2 sample). Note that the flow-induced birefringence images acquired during a steady state for two polystyrene samples were presented in Castro et al. (2018) together with the determination of fringe order (k).

Figure 29 shows a comparison for GPPS1 and GPPS2 samples of the measurements obtained with the GIMP software and also those acquired with the proposed morphological approach. The values for the principal stress difference module along the flow centerline, which is depicted as the red-dashed line in Fig. 23, were calculated using Eq. 1.

As mentioned previously (Castro et al. 2018; Farias et al. 2014), the flow in the slit die is characterized by two regions: (i) the inlet in which PSD values reach the maximum and (ii) the exit region in which the PSD value is zero. These regions correspond, respectively to the maximum value of k next to fringe position = 0 mm, which is the spatial region where molten polymer reaches the geometry channel, and to the value of $k = 0$ that corresponds to channel length (fringe position = 5 mm). In this point, the change in the main flow direction occurs and consequently, the signal inversion of the PSD values is observed, justifying the minimum point of the |PSD| in the value equal to zero (Castro et al. 2018; Lord et al. 2010). For a visualization of the geometry of the experiment, one can refer to Fig. 23.

According to the figures, it is possible to observe that the results obtained with the proposed methodology presented good agreement with the results obtained with the GIMP software, and the proposed methodology was able to determine the points with maximum retardation order, which are related to the fringe position = 0 mm, for all the experiments, with the exception of the experiment for the sample GPPS2 carried out at 0.2 mm/s (Fig. 29d). In this case, the proposed methodology was not able to properly detect the fringe $k = 8$, due to the overlap of fringes $k = 7$, and $k = 8$ in the image.

The standard deviation (S) of the fringe positions for both techniques is presented in Figs. 30 and 31. It is possible to observe in Figs. 30b and 31b, which represent the proposed image processing-based approach via mathematical morphology, a more predictable behavior of the standard

Fig. 31 Standard deviation S as a function of distance along the centerline for the sample GPPS2. The centerline is depicted as the red-dashed line in Fig. 23. **a** Manual method (GIMP). **b** Proposed morphological approach

(a)

(b)
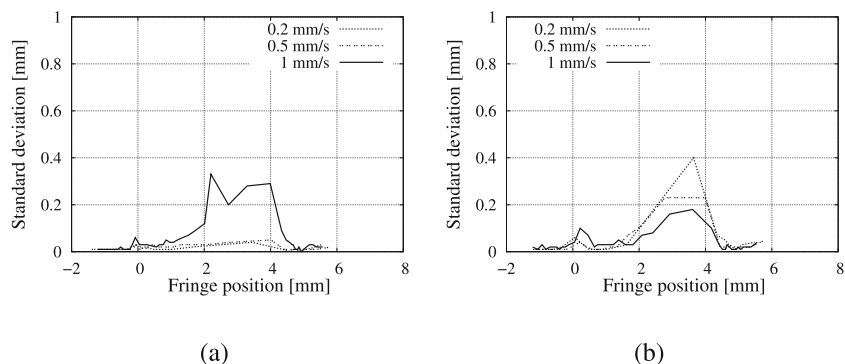
deviation. For these cases, the highest values of standard deviation are between the middle and the exit of the slit, that is, approximately between fringe position = 2 and 4 mm. Also, experiments with lower velocities, therefore with larger fringes and a lower number of fringes per image, show, in general, larger values of standard deviation. On the other hand, for the GIMP approach, there is no simple pattern for the standard deviation since it also depends on subjective factors. These observations suggest that the morphological approach helps to increase reproducibility of the results. In addition, the full processing of 15 images, together with the statistical treatment of the results, takes around 30 s. With the GIMP software, the processing must be performed for one image at a time, taking around 8 min for determination of the dark fringe centers for the 15 images tested.

At this point, it is important to analyze the results more closely, particularly in the cases of large deviations, where the values for distance of dark fringe centers are less accurate. These are observed in the following cases for the proposed automatic technique:

1. Inflection points for the fringe order
2. Fringes without definition, which is related to image quality
3. Fringes stretched along the slit-die, a deformation that happens in reported region between the middle and the exit of the slit
4. Fringes superimposed, which is the case when two fringes may appear visually indistinguishable

5. Fringes in the border, when the dark fringe is in the image border and does not always appear surrounded by bright fringes

In order to determine whether the observed differences in fringe positions obtained with the two techniques are significant or not, a statistical analysis was performed, based on the f-distribution, aimed at evaluating variances and unpaired Student's t distribution (Montgomery and Runger 2013) , considering that there is no dependence between methodologies. The analyses were done with confidence level of 95% in the R software (R Development Core Team 2008). In this way, the difference between the average of the fringe positions ($D_{\bar{x}}$) obtained by the GIMP and the proposed morphological approach, as well as the respective confidence interval were determined. Figure 32 presents the results obtained for the experiment carried out at 0.5 mm/s for GPPS1 sample, in which the numbers 2, 3, 4, 5, 4, 3, 2, 1, 0, 1, 2, 3, and 2 represent the fringe retardation order (k) indicated in Fig. 33, which is related to an ordering and counting of the dark fringes. The results indicate that $D_{\bar{x}}$ is very close or equal to zero for all fringes. Additionally, the calculated confidence interval crosses a region of difference equal to or close to zero.

The analyses for the experiments performed at 1 and 2 mm/s with GPPS1 sample and at 0.2, 0.5, and 1 mm/s for the GPPS2 sample can be found in the supplementary material (http://www02.smt.ufrj.br/eduardo/birefringence/). There one can also find the detailed measurements with their respective standard deviations, as well as a list of

Fig. 32 Statistical analysis for GPPS1 0.5 mm/s based on Student's t distribution: difference between the average distance of fringe centers obtained by the manual marking (GIMP) and the morphological approach, in function of the fringe order, together with the corresponding 95% confidence interval
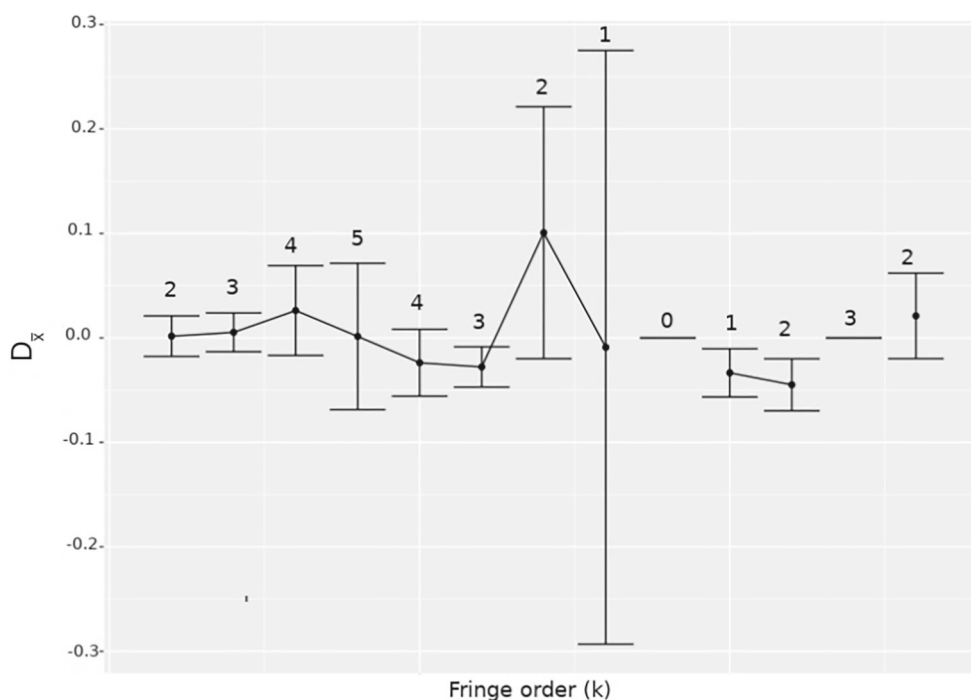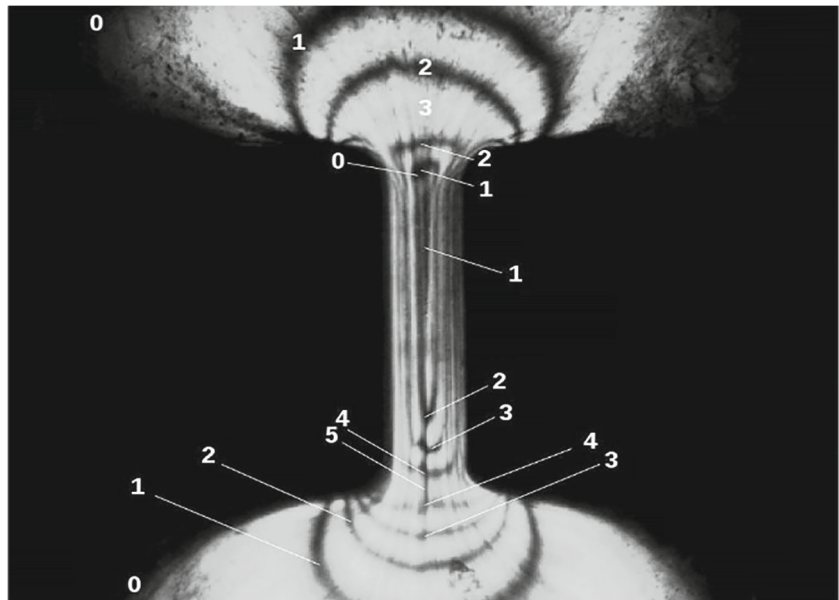
Fig. 33 Fringe retardation order
(*k*) of sample GPPS1 at
0.5 mm/s (Castro et al. 2018)

occurrences of large deviations in the results. In all cases, $D_{\bar{x}}$ is in a region close to zero for most of the fringes, showing that in general, the proposed method is able to provide result consistent with the one given by the GIMP approach.

Conclusions

In this work, a novel approach to the problem of detecting the position of dark fringes in flow-induced birefringence images obtained during the melt flow in the multipass rheometer was presented and applied for a sample of polystyrene. The proposed methodology allows fast and accurate measurements of the dark fringe centers. In addition, it is an automatic method, which provides the minimum human intervention in the image processing, in contrast to the semi-automatic methodology using GIMP software, presented in previous work, in which the user must interfere directly in the measurements. The obtained results have been shown to be consistent with those of semi-automatic detection using the GIMP software, with the advantage of a smaller variance of the measurements.

One should also bear in mind that the amount of time taken to correct those easily identifiable mistakes of the algorithm is still much smaller than the one it takes to perform all the measurements using the GIMP methodology. The obtained results indicate that the proposed method is a reliable alternative to the manual (and semi-automatic) methods currently in use, as it is able to perform the detection of the positions with high confidence and in a faster way than the alternative methods.

It should be noted that most of the deviation observed is due to problems in the image acquisition, which causes some fringes to have a low contrast and also make consecutive fringes to appear mixed in the recorded image. This problem can be solved with improvements in the experiments, such as lens adjustments in which the passage of polarized light is changed, thus enhancing the quality of the images, allowing clearer and more defined fringes. It is important to point out that the technique developed in this paper is able to provide information about the fringe positions even in the case where the images are polluted by impurities, providing an even better performance in higher quality images. This, in our opinion, is a strong indication of the potential advantages of the proposed methodology.

References

Agassant JF, Mackley MR (2015) A personal perspective on the use of modelling simulation for polymer melt processing. Int Polym Process 30:121–140

Agassant JF, Baaijens F, Bastian H, Bernnat A, Bogaerds A, Coupez T, Debbaut B, Gavrus AL, Goublomme A, Van Gurp M et al (2002) The matching of experimental polymer processing flows to viscoelastic numerical simulation. Int Polym Process 17(1):3–10

Ahmed R, Liang R, Mackley M (1995) The experimental observation and numerical prediction of planar entry flow and die swell for molten polyethylenes. J Non-Newtonian Fluid Mech 59(2):129–153

Beucher S, Lantuéj C (1979) Use of watersheds in contour detection. In: International workshop on image processing, real-time edge and motion detection

Castro AM, Pereira JO, Farias TM, Secchi AR, Cardozo NSM (2018) Application of the GIMP software in the analysis of birefringence images obtained in a multipass rheometer. Rheol Acta 57(2):113–126

Collis M, Mackley M (2005) The melt processing of monodisperse and polydisperse polystyrene melts within a slit entry and exit flow. J Non-Newtonian Fluid Mech 128(1):29–41

EL-Morsy M (2012) A new algorithm for automatic double bright fringe of multiple-beam fizeau fringe skeletonization using Fourier transform method of fringe pattern analysis. J Signal Inf Process 3(3):412–419

Farias TM, Secchi AR, Butler S, Cardozo NSM (2014) Utilizaċão da técnica de birrefringência em reômetro multipasse para a diferenciaċão de grades de poliestireno cristal. Polímeros 24(5):596–603

Farooq M, Aslam A, Hussain B, Hussain G, Ikram M (2015) A comparison of image processing techniques for optical interference fringe analysis. Photonic Sensors 5(4):304–311

Fuller GG (1995) Optical rheometry of complex fluids. Oxford University Press, Inc, New York

Fulong D, Wang Z (1999) Automatic fringe patterns analysis using digital processing techniques: I. Fringe center method. Acta Photonica Sinica 28(8):700–6

Haralick RM, Shapiro LG (1992) Computer and robot vision, 1st edn. Addison-Wesley Longman Publishing Co., Inc., Boston

Harrison P, J P Janssen L, P Navez V, Peters G, Baaijens F (2002) Birefringence measurements on polymer melts in an axisymmetric flow cell. Rheol Acta 41:114–133

Hassell DG, Mackley MR (2009) An experimental evaluation of the behaviour of mono and polydisperse polystyrenes in cross-slot flow. Rheol Acta 48(5):543–550

Hassell DG, Auhl D, McLeish TCB, Mackley MR (2008) The effect of viscoelasticity on stress fields within polyethylene melt flow for a cross-slot and contraction–expansion slit geometry. Rheol Acta 47(7):821–834

Hassell DG, Lord TD, Scelsi L, Klein DH, Auhl D, Harlen OG, McLeish TCB, Mackley MR (2011) The effect of boundary curvature on the stress response of linear and branched polyethylenes in a contraction–expansion flow. Rheol Acta 50(7):675–689

Huntley JM (1998) Automated fringe pattern analysis in experimental mechanics: a review. J train Analys Eng Des 33(2):105–125

Lee K, Mackley M (2000) The significance of slip in matching polyethylene processing data with numerical simulation. J Non-Newtonian Fluid Mech 94(2):159–177

Lee K, Mackley M (2001) The application of the multi-pass rheometer for precise rheo-optic characterisation of polyethylene melts. Chem Eng Sci 56(19):5653–5661

Lord TD, Scelsi L, Hassell DG, Mackley MR, Embery J, Auhl D, Harlen OG, Tenchev R, Jimack PK, Walkley MA (2010) The matching of 3D rolie-poly viscoelastic numerical simulations with experimental polymer melt flow within a slit and a cross-slot geometry. J Rheol 54(2):355–373

Mackley M, Hassell D (2011) The multipass rheometer a review. J Non-Newtonian Fluid Mech 166(9):421–456

Macosko CW, Larson RG (1994) Rheology: principles, measurements, and applications, 1st edn. Wiley, New York

MATLAB (2012) version R2012b. The MathWorks Inc., Natick

Meyer F (1979) Iterative image transformations for an automatic screening of cervical smears. J Histochem Cytochem 27(1):128–135

Montgomery DC, Runger GC (2013) Applied statistics and probability for engineers. Wiley, New York

Poon CY, Kujawinska M, Ruiz C (1993) Automated fringe pattern analysis for moiré interferometry. Exp Mech 33(3):234–241

R Development Core Team (2008) R: a language and environment for statistical computing R foundation for statistical computing, Vienna, Austria

Reynolds C, Thompson R, McLeish T (2018) Pressure and shear rate dependence of the viscosity and stress relaxation of polymer melts. J Rheol 62(2):631–642

Serra J (1983) Image analysis and mathematical morphology. Orlando, Academic Press Inc.

Soille P (2003) Morphological image analysis: principles and applications, 2nd edn. Springer-Verlag, New York

Sokkar T, Dessouky HE, Shams-Eldin M, El-Morsy M (2007) Automatic fringe analysis of two-beam interference patterns for measurement of refractive index and birefringence profiles of fibres. Opt Lasers Eng 45(3):431–441

Thomaz LA, da Silva AF, da Silva EAB, Netto SL, Castro AM, Pereira JO, Secchi AR (2016) A morphological approach to the automatic detection of dark fringes applied to birefringence images. In: 2016 IEEE international conference on image processing (ICIP), Phoenix, USA, pp 739–743

Wang Z, Han B (2004) Enhanced random phase shifting technique In: X SEM International Congress & Exposition on Experimental & Applied Mechanics, Costa Mesa, USA

Ye G, Wei L (2012) A method for interference fringe fast skeletonizing. In: 2nd international conference on computer science and network technology, Changchun, China, pp 1784–1786

Yu Q, Andresen K (1994) Fringe-orientation maps and fringe skeleton extraction by the two-dimensional derivative-sign binary-fringe method. Appl Opt 33(29):6873–6878

Yu Q, Liu X, Andresen K (1994) New spin filters for interferometric fringe patterns and grating patterns. Appl Opt 33(17):3705–3711

Zhang D, Ma M, Arola DD (2002) Fringe skeletonizing using an improved derivative sign binary method. Opt Lasers Eng 37(1):51–62